Main Manuscript for

Microtubule assembly by soluble tau impairs vesicle endocytosis and excitatory neurotransmission via dynamin sequestration in Alzheimer's disease mice synapse model

Tetsuya Hori,[1,2] Kohgaku Eguchi,[1,4], Han-Ying Wang,[1] Tomohiro Miyasaka,[2] Laurent Guillaud,[1,5] Zacharie Taoufiq,[1] Satyajit Mahapatra,[1] Hiroshi Yamada,[3] Kohji Takei,[3] Tomoyuki Takahashi[1*]

[1]Cellular and Molecular Synaptic Function Unit, Okinawa Institute of Science and Technology Graduate University, Okinawa 904-0495, Japan.

[2]Faculty of Life and Medical Sciences, Doshisha University, Kyoto 610-0394, Japan.

[3]Department of Neuroscience, Graduate school of Medicine, Dentistry and Pharmaceutical Sciences, Okayama University, Okayama 700-8558, Japan.

[4]Institute of Science and Technology Austria (IST Austria), Am Campus 1, A-3400 Klosterneuburg, Austria

[5]Molecular Neuroscience Unit, Okinawa Institute of Science and Technology Graduate University, Okinawa 904-0495, Japan.

*Tomoyuki Takahashi.

Email: ttakahas@oist.jp

Competing Interest Statement: The authors declare no competing financial interests.

Classification: BIOLOGICAL SCIENCES: Neuroscience

Keywords: Tau; Calyx of Held Presynaptic Terminal; Microtubule; Dynamin; Endocytosis.

This PDF file includes:

Main Text
Figures 1 to 5
There are no Tables in this PDF file

Abstract

Elevation of soluble wild-type (WT) tau occurs in synaptic compartments in Alzheimer's disease. We addressed whether tau elevation affects synaptic transmission at the calyx of Held in slices from mice brainstem. Whole-cell loading of WT human tau (h-tau) in presynaptic terminals at 10-20 μM caused microtubule (MT) assembly and activity-dependent rundown of excitatory neurotransmission. Capacitance measurements revealed that the primary target of WT h-tau is vesicle endocytosis. Blocking MT assembly using nocodazole prevented tau-induced impairments of endocytosis and neurotransmission. Immunofluorescence imaging analyses revealed that MT assembly by WT h-tau loading was associated with an increased MT-bound fraction of the

endocytic protein dynamin. A synthetic dodecapeptide corresponding to dynamin-1-pleckstrin-homology domain inhibited MT-dynamin interaction and rescued tau-induced impairments of endocytosis and neurotransmission. We conclude that elevation of presynaptic WT tau induces *de novo* assembly of MTs, thereby sequestering free dynamins. As a result, endocytosis and subsequent vesicle replenishment are impaired, causing activity-dependent rundown of neurotransmission.

Significance Statement

Wild-type human recombinant tau loaded in rodent presynaptic terminals inhibited vesicle endocytosis, thereby causing activity-dependent rundown of excitatory transmission. This endocytic block is caused by a sequestration of dynamin by excess microtubules newly assembled by tau and can be rescued by a peptide inhibiting the microtubules-dynamin interaction, or by the microtubule disassembler nocodazole. Thus, synaptic dysfunction can be induced by pathological increase of endogenous soluble tau in Alzheimer disease slice model.

Main Text

Introduction

The microtubule (MT) binding protein tau assembles and stabilizes MTs (1, 2) mainly in axonal compartments (3, 4). Phosphorylation of tau proteins reduces their binding affinity (5, 6), thereby shifting the equilibrium from MT-bound form to soluble free form (7). Soluble tau proteins also exist in dynamic equilibrium between phosphorylated and dephosphorylated forms (8) as well as between soluble and aggregated forms. When the cytosolic tau concentration is elevated, monomeric tau undergoes oligomerization and eventually precipitates into neurofibrillary tangles (NFT) (9-11), which is a hallmark of tauopathies, including Alzheimer's disease (AD), frontotemporal dementia with Parkinsonism-17 (FTDP-17) and progressive supranuclear palsy (PSP) (2, 7, 8). Although the NFT density can correlate with the degree of AD progression (2, 7, 12), soluble tau protein levels are more closely linked to disease progression and cognitive decline (13, 14).

Genetic ablation of tau shows little abnormal phenotype (15-17), presumably due to compensation by other MT-associated proteins (15). Instead, tau ablation can prevent amyloid β-induced impairments of mitochondrial transport (16) or memory defects (18, 19). Thus, loss of tau function due to its dissociation from MTs is unlikely to be an important cause of neuronal dysfunction in AD (8, 12).

In postmortem brains of both AD patients and intact humans, tau is present in synaptosomes (20, 21). In a transgenic mice AD model, soluble tau is accumulated in the hippocampal nerve terminal zone (22, 23). Both *in vivo* and in culture models of tauopathy, tau is released from axon terminals upon KCl stimulation in a Ca^{2+}-dependent manner, like neurotransmitters (24, 25). Tau oligomers produced by released tau triggers endogenous tau seeding in neighboring neurons, thereby causing trans-synaptic propagations (22, 26).

FTDP tauopathy model mice that overexpressed with mutant tau are widely used to examine tau toxicities on synaptic plasticity (27-29), memory formation (28, 30) as well as on synaptic vesicle transport (31, 32). In contrast to FTDP, which is a rare familial disease associated with tau mutation, AD is a widespread sporadic disease unassociated with tau mutation, but the expression level of WT tau being crucial. As AD models, the effects of WT tau overexpression have been examined in culture cells (33-36) or in *Drosophila* (37), where impaired axonal transports associated with increased MT density were found. These observations suggest that WT tau can be detrimental when its levels are elevated (35, 36). However, unlike FTDP tau mutant, it is unknown whether elevated soluble WT tau can affect mammalian central synaptic transmission.

We addressed this question using the giant nerve terminal calyx of Held visualized in slices from mice brainstem, where axonal MTs extended into the depth of terminals (38). In this

presynaptic terminal, we loaded recombinant WT h-tau from a whole-cell patch pipette at fixed concentrations to model the elevation of WT tau associated with AD and found that WT h-tau newly assembled MTs and strongly impaired synaptic transmission. Capacitance measurements indicated that the primary target of WT h-tau is vesicle endocytosis. Immunocytochemical image analysis after cell permeabilization revealed an increase in the MT-bound fraction of the endocytic GTPase dynamin in WT h-tau-loaded terminals. Since the endocytic key protein dynamin is a MT-binding protein (39), dynamin is likely sequestered by newly assembled MTs. Out of screening, we found that a synthetic dodecapeptide corresponding to amino acids 560-571 of dynamin 1 inhibited MT-dynamin interaction. When we co-loaded this peptide "PHDP5" with WT h-tau, its toxicities on vesicle endocytosis as well as on synaptic transmission were rescued. Thus, we propose a novel synaptic dysfunction mechanism underlying AD, in which WT tau-induced over-assembly of MTs depletes dynamins, thereby impairing vesicle endocytosis and synaptic transmission.

Results

Intra-terminal loading of WT h-tau impairs excitatory synaptic transmission

To address whether elevation of soluble h-tau in presynaptic terminals can affect synaptic transmission, we purified WT recombinant h-tau (0N4R) and its deletion mutant (del-MTBD) lacking the MT binding site (244Gln-367Gly) (Figure 1 – figure supplement 1A), obtained using an *E. coli* expression system (40). These recombinant h-tau proteins are highly soluble at room temperature without any sign of granulation (41). In simultaneous pre- and postsynaptic recording at the calyx of Held in mouse brainstem slices, we recorded EPSCs evoked at 1 Hz by presynaptic action potentials (Figure 1). After confirming stable EPSC amplitude for 10 min, we injected a large volume of internal solution containing WT h-tau (20 μM) from an installed fine tube to a presynaptic whole-cell pipette to replace most of pipette solution and allow h-tau to diffuse into a presynaptic terminal (illustration in Figure 1A) (42, 43). After loading h-tau (20 μM), the amplitude of glutamatergic EPSCs gradually declined and reached 23 ± 9 % in 30 min (Figure 1A, $p < 0.01$, paired t-test, n = 6 synapses in 6 slices). WT h-tau loaded at a lower concentration (10 μM) caused a slower EPSC rundown to 65 ± 5 % in 30 min ($p < 0.01$, n = 5 synapses in 5 slices). Del-MTBD (20 μM), lacking tubulin polymerization capability (Figure 1 – figure supplement 1B), likewise loaded had no effect on EPSC amplitude (Figure 1A). Since h-tau concentrations in presynaptic terminals are equilibrated with those in a presynaptic whole-cell pipette with a much greater volume than terminals (44), these results suggest that WT h-tau >10 μM can significantly impair excitatory synaptic transmission.

The inhibitory effect of WT h-tau on EPSCs was apparently frequency-dependent. When evoked at 0.1 Hz, WT h-tau (20 μM) caused only a minor reduction of EPSC amplitude (to 85 ± 12 %, 30 minutes after loading, $p = 0.21$, n = 5; Figure 1B). Since taxol shares a common binding site of MTs with tau (45) and assembles tubulins into MTs (Figure 1 – figure supplement 1B), we tested the effect of taxol (1 μM) on EPSCs (Figure 1C). Like h-tau, taxol caused a significant rundown of EPSCs evoked at 1 Hz (to 41 ± 12 at 30 min, n =5, $p< 0.05$), but not those evoked at 0.1 Hz (104 ± 3.0 %, n = 4, $p = 0.60$). These results together suggest that MTs newly assembled in presynaptic terminals by WT h-tau or taxol cause activity-dependent rundown of excitatory synaptic transmission.

WT h-tau primarily inhibits SV endocytosis and secondarily exocytosis

To determine the primary target of h-tau causing synaptic dysfunction, we performed membrane capacitance measurements at the calyx of Held (46-49). Since stray capacitance of perfusion pipettes prevents capacitance measurements, we backfilled h-tau into a conventional patch pipette after preloading normal internal solution only at its tip to secure GΩ seal formation. This caused substantial and variable delays of the intra-terminal diffusion, so no clear effect could be seen more than 10 minutes after whole-cell patch membrane was ruptured. 20 minutes after whole-cell patch-loading of WT h-tau (20 μM), endocytic capacitance showed a significant

slowing (Figure 2), whereas exocytic capacitance magnitude (ΔC_m) or charge of Ca^{2+} currents (Q_{Ca}) induced by a depolarizing pulse was not different from controls without h-tau loading. 30 minutes after loading h-tau, the endocytic capacitance change became further slowed ($p < 0.01$), and exocytic ΔC_m eventually showed a significant reduction ($p < 0.05$, $n = 5$) without a change in Q_{Ca}. These results suggest that the primary target of h-tau toxicity is synaptic vesicle (SV) endocytosis. Endocytic block inhibits recycling replenishment of SVs via recycling, thereby reducing the exocytic release of neurotransmitter as a secondary effect.

Inhibition of SV endocytosis and synaptic transmission by WT h-tau requires *de novo* MT assembly

Since new MT assembly might take place after h-tau loading (Figure 1, Figure 1 – figure supplement 1), we tested whether the tubulin polymerization blocker nocodazole might reverse the toxic effects of h-tau on SV endocytosis and synaptic transmission. In tubulin polymerization assays, nocodazole inhibited h-tau-dependent MT assembly in a concentration-dependent manner, with a maximal inhibition reached at 20 μM (Figure 3A). In presynaptic capacitance measurements, nocodazole (20 μM) co-loaded with h-tau (20 μM) fully prevented the h-tau toxicities on endocytosis (Figure 3B) and synaptic transmission (Figure 3C). Nocodazole alone (20 μM) had no effect on exo-endocytosis (Figure 3B) or EPSC amplitude (Figure 3C). It is highly likely that WT h-tau loaded in calyceal terminals newly assembled MTs, thereby impairing SV endocytosis and synaptic transmission.

WT h-tau assembles MTs and sequesters dynamins in calyceal terminals

The monomeric GTPases dynamin 1 and 3 play critical roles in the endocytic fission of SVs (50-52). Since dynamin is originally discovered as a MT-binding protein (39), we hypothesized that newly assembled MTs might trap free dynamins in cytosol. If this is the case, MT-bound form of dynamin would be increased. To test this hypothesis, we performed immunofluorescence microscopy and image analysis to quantify MTs and dynamin. After whole-cell infusion of h-tau into calyceal terminals, slices were chemically fixed and permeabilized to allow cytosolic free molecules such as tubulin monomers to be washed out of the terminal, thereby enhancing the signals from large structures such as MTs or MT-bound molecules. Fluorescent h-tau antibody identified calyceal terminals loaded with WT h-tau (20 μM, Figure 4A). Double staining with mouse β3-tubulin antibody revealed a 2.1-fold increase in MT signals in h-tau-loaded terminals, compared with those without h-tau loading ($p = 0.01$, $n = 5$, two-tailed unpaired t-test with Welch's correction, Figure 4B). Triple labeling with dynamin antibodies further revealed a 2.6-fold increase in dynamin signal ($p = 0.01$, $n = 5$, two-tailed t-test with Welch's correction, Figure 4B). In super-resolution imaging, dynamins are shown in clusters along MTs in tau-loaded calyceal terminal (Figure4 –figure supplement 1). These results suggest that soluble WT h-tau can assemble MTs in presynaptic terminals, thereby sequestering cytosolic dynamins that are indispensable for SV endocytosis.

Besides dynamins, MTs can bind to various other proteins. Among them, formin mDia can bind to MTs (53) and involved in the endocytic scaffold functions together with F-actin, intersectin and endophilin. Although acute depolymerization of F-actin (38, 46) or genetic ablation of intersectin (54) has no effect on SV endocytosis at the calyx of Held, the formin mDia inhibitor SMFH2 reportedly inhibits endocytosis at the calyx terminals in pre-hearing rats (postnatal day [P] 8-12) (55). We re-examined whether the drug might inhibit SV endocytosis at calyceal terminals in slices from post-hearing mice (P13-14). SMFH2 slightly prolonged SV endocytosis, but this effect was statistically insignificant (Figure4 –figure supplement 2A). Thus, formin unlikely makes substantial contribution to the marked endocytic slowing observed after intra-terminal tau loading (Figure 2).

It may also be argued that binding of endophilin to MTs (56) might cause EPSC rundown since endophilin is involved in clathrin uncoating (57), which is required for SV refilling with glutamate. If SV refilling during recycling is impaired, miniature EPSCs are decreased in amplitude and frequency(58). However, neither amplitude nor frequency was affected by intra-

terminal loading of tau (20 μM) (Figure4 –figure supplement 2B). Thus, endophilin-MT binding unlikely underlies EPSC rundown by intra-terminal tau infusion (Figure 1).

A microtubule-dynamin binding inhibitor peptide attenuates h-tau toxicities on SV endocytosis and synaptic transmission

To prevent toxic effects of h-tau on endocytosis and transmission, we searched for a dominant-negative (DN) peptide blocking MT-dynamin binding. Since the MT binding domain of dynamins is unknown, we synthesized 11 peptides from the pleckstrin-homology (PH) domain and 11 peptides from the proline-rich domain of dynamin 1 (Figure4 –figure supplement 1A) and submitted them to the MT-dynamin1 binding assay. Out of 22 peptides, one peptide corresponding to the amino acid sequence 560-571 of PH domain, which we named "PHDP5", significantly inhibited the MT-dynamin 1 interaction (Figure 5A, Figures5 –figure supplement 1B and C). By SYPRO orange staining, dynamin 1 is found as a ~100 kDa band, 1.7 ± 0.4 % in precipitates (ppts). In the presence of MT, dynamin 1 in ppts increased to 22.6 ± 2.4 %, indicating sequestration of dynamin 1 by MTs. When PHDP5 was added to MT and dynamin 1, dynamin1 in the ppt fraction decreased to 6.3 ± 2.4 %, indicating that PHDP5 works as a DN peptide for inhibiting MT-dynamin interactions (Figure 5A).

A cryo-electron microscope study on dynamin 1 assembled on lipid membrane has revealed that PH domain is tucked up into dynamin structure in apo state, but upon GTP binding, exposed toward membrane by a conformational change (59). In negatively stained electron micrographs, dynamin 1 is periodically arranged on the surface of MTs (60), suggesting a helical polymerization like in dynamin-membrane interaction (61). Therefore, PH domain including the putative binding site PHDP5 is likely exposed toward MT surface. To examine whether PH domain of dynamin 1 can directly bind to MTs, immunofluorescence labelled MTs and glutathione transferase-tagged PH domain (GST-PH) were mixed and observed by confocal and electron microscopy (Figure5 –figure supplement 2). In confocal microscopic imaging, GST-PH co-localized with MTs, in contrast to controls, where MTs were mixed with GST alone (Figure5 –figure supplement 2A). These results were further confirmed in electron microscopic imaging, showing co-localizations of MTs and GST-PH (Figure5 –figure supplement 2B). Thus, dynamin 1 PH domain can associate with MTs, although it remains to be determined whether PHDP5 can directly bind to MTs.

Loading of PHDP5 (0.25 mM) alone in calyceal terminals had no effect on exo-endocytic capacitance changes, but when co-loaded with WT h-tau (20 μM), it significantly attenuated the h-tau-induced endocytic slowing ($p < 0.05$, Figure 5B). Scrambled PHDP5 peptide (0.25 mM) loaded as a control had no effect on h-tau-induced endocytic slowing. Like its effect on capacitance changes, intra-terminal infusion of PHDP5 alone (1 mM) did not affect EPSC amplitude, but when co-loaded with WT h-tau (20 μM), significantly attenuated the inhibitory effect of h-tau on EPSC amplitude ($p < 0.01$, Figure 5C). Co-infusion of scrambled PHDP5 (1 mM) with h-tau (20 μM) did not affect the h-tau-induced EPSC rundown ($p = 0.46$). These results further support that WT h-tau causes dynamin deficiency via new assembly of MTs thereby impairing SV endocytosis and synaptic transmission. These results also highlight PHDP5 as a potential therapeutic tool for rescuing synaptic dysfunctions associated with AD or PD.

Discussion

Using the calyx of Held in brainstem slices as an AD model for dissecting mammalian central excitatory synaptic transmission, we demonstrated that intra-terminal loading of WT h-tau impairs vesicle endocytosis and synaptic transmission via *de novo* MT assembly. Previous over-expression studies in cultured cells reported MT assembly by injection or overexpression of WT tau (36, 62, 63) or phosphorylated tau (34, 64). Compared with overexpression, our whole-cell method allows targeted loading of molecules in presynaptic terminals at defined concentrations because of a large pipette-to-cell volume ratio (44). In postmortem brain tissue homogenates from AD patients, soluble tau content is estimated as 6 ng/μg of protein, which is 8 times higher

than controls (65). Assuming protein contents in brain homogenate as 10%, 60 kDa tau concentration in AD patients' brain is estimated as 10 μM. Since elevation of soluble tau concentration likely occurs mainly in axons and axon terminal compartments of neurons, soluble tau concentration in AD patients in presynaptic terminals can be higher than that. Our results at the calyx of Held suggest that excitatory synaptic transmission, in general, can be significantly impaired in such situations. In fact, the magnitude of EPSC rundown after WT h-tau loading is comparable to that caused by the clinical dose of general anesthetic isoflurane at the calyx of Held in slice (48). In AD, tau pathology starts from the locus coeruleus in the brainstem and undergoes trans-synaptic propagation to hippocampal and neocortical neurons (66). Present results in our model synapse suggest that synaptic functions in such tau-propagation pathways can be severely affected at the early stage of AD.

Membrane capacitance measurements at the calyx of Held revealed the primary target of WT h-tau toxicity as SV endocytosis. Endocytic slowing impairs SV recycling and reuse, thereby inhibiting SV exocytosis, particularly in response to high-frequency stimulations (49). The toxic effects of h-tau on SV endocytosis and synaptic transmission were prevented by nocodazole co-application. Together with the lack of toxicity of del-MTBD and toxic effects of taxol on synaptic transmission, these results suggest pathological roles of over-assembled MTs. Like WT h-tau, intra-terminal loading of WT α-synuclein slows SV endocytosis and impairs fidelity of high-frequency neurotransmission at the calyx of Held (46). α-Synuclein toxicities can be rescued by blocking MT assembly with nocodazole or a photosensitive colchicine derivative PST-1. Thus, a common mechanism likely underlies synaptic dysfunctions in AD and PD. Compared with α-synuclein, h-tau toxicity is much stronger on endocytosis as well as on synaptic transmission. Thus, abnormal elevation of endogenous molecules beyond homeostatic level may cause AD and PD symptoms, like many other human diseases.

Although the GTPase dynamin is a well-known player in endocytic fission of SVs (50, 52), it was originally discovered as a MT-binding protein (39). Subsequent studies indicated that this interaction upregulates dynamin's GTPase activity (67, 68) and can induce MT instability with dynamin 2 (69) or stabilizes MT bundle formation with dynamin 1 (60). However, the binding domain of dynamin remained unidentified. In this study, calyceal terminals loaded with WT h-tau showed a prominent increase in immunofluorescence signal intensity corresponding to bound dynamins. This was associated with an elevation in intra-terminal MTs, suggesting that newly assembled MTs induced by loaded h-tau sequestered cytosolic dynamins. These results well explain impairments of SV endocytosis by intra-terminal h-tau loading. Through synthetic peptide screening, we found that a dodecapeptide from dynamin 1 PH domain significantly inhibited the MT-dynamin interaction. This peptide PHDP5 is ~80 % homologous to dynamin 3, another isoform involved in vesicle endocytosis (51). Although direct binding of this peptide to MTs remains to be seen, it significantly rescued endocytic impairments and EPSC rundown induced by intra-terminal WT h-tau. Hence, MTs over-assembled by soluble WT h-tau proteins likely sequester free dynamins in presynaptic terminals, thereby blocking SV endocytosis and synaptic transmission, at least in this slice model. This dynamin sequestration mechanism by newly assembled MTs may also underlie the toxic effect of α-synuclein on SV endocytosis (46) in PD.

Unlike WT h-tau, the FTDP-linked mutant tau does not affect SV endocytosis (32), but binds to both actin filaments (70) and the SV transmembrane protein synaptogyrin (31), thereby immobilizing SVs (31, 32). WT-tau can also bind to synaptogyrin (31), but cannot bind to F-actins because of a difference in the MT-binding regions between FTDP mutant and WT tau (62, 71). However, WT h-tau can bind to various other macromolecules and organelles such as MTs, neurofilaments and ribosomes (72) as well as to synaptogyrin, thereby possibly immobilizing SVs. Recycling transport of SVs impaired by this mechanism might additionally contribute to the rundown of synaptic transmission remaining unblocked by the MT-dynamin blocker peptide.
In the absence of a powerful tool for alleviating symptoms associated with AD or PD, the calyx of Held slice model might provide a platform upon which therapeutic tools for rescuing synaptic dysfunctions can be pursued. The combination of this slice model with animal models could provide a new pathway toward rescuing neurological disorders.

Materials and Methods

Animals

All experiments were performed in accordance with the guidelines of the Physiological Society of Japan and animal experiment regulations at Okinawa Institute of Science and Technology Graduate University.

Recombinant human tau preparation

Human tau (h-tau) lacking the MT-binding domain (amino acid 244 to 367, del-MTBD) were produced by site-directed mutagenesis as previously reported (40). Wild-type (WT) and del-MTBD mutant h-tau of 0N4R isoform were expressed in *E. coli.* (BL21/DE3) and purified as described previously (73) with minor modifications. Briefly, harvested bacteria expressing recombinant tau were lysed in homogenization buffer (50 mM PIPES, 1 mM EGTA, 1 mM DTT, 0.5 mM PMSF, and 5 μg/ml Leupeptin, pH6.4), sonicated and centrifuged at 27,000 xg for 15 min. Supernatants were charged onto phosphocellulose column (P11, Whatman). After washing with homogenization buffer containing 0.1 M NaCl, h-tau-containing fractions were eluted by the buffer containing 0.3 M NaCl. Subsequently, the proteins were precipitated by 50 % saturated ammonium sulfate and re-solubilized in homogenization buffer containing 0.5 M NaCl and 1% 2-mercaptoethanol. After incubation at 100 °C for 5 min, heat stable (soluble) fractions were obtained by centrifugation at 21,900 xg, and fractionated by reverse phase high-performance liquid chromatography (RP-HPLC) using Cosmosyl Protein-R (Nacalai tesque Inc.). Aliquots of h-tau containing fractions were lyophilized and stored at -80 °C. Purified h-tau proteins were quantified by SDS-PAGE followed by Coomassie Brilliant Blue staining.

Purification of recombinant human dynamin1 protein

His-tagged human dynamin 1 was expressed using the Bac-to-Bac baculovirus expression system (Thermo Fisher Scientific, Waltham, MA, USA) and purified as described previously (74). The purified dynamin solutions were concentrated using Centriplus YM50 (cat#4310; Merck-Millipore, Darmstadt, Germany).

Microtubule polymerization assay

Effects of tau and nocodazole on MT polymerization were tested using a Tubulin Polymerization Assay (Cytoskeleton Inc., Denver, CO). Briefly, purified WT or del-MTBD mutant h-tau (10 μM) were mixed with porcine tubulin (20 μM) in an assembly buffer at 37 °C. Nocodazole was added to the mixture at 0 min of incubation. MT polymerization was fluorometrically assayed (excitation at 360 nm, emission at 465 nm) using Infinit F-200 Microplate Reader (TECAN, Männedorf / Switzerland) at 1 min intervals for 30 min. After incubation, resultant solutions were subjected to centrifugation at 100,000 xg for 15 min at 20°C. Supernatants (free tubulin fraction) and pellets (microtubule fraction) were subjected to SDS-PAGE to quantify the amount of tubulin assembled into MTs.

Peptide synthesis and LC-MS/MS analysis

The peptides were synthesized through conventional 9-fluorenylmethyloxycarbonyl (Fmoc) solid-phase peptide synthesis (SPPS), onto preloaded Fmoc-alanine TCP-resins (Intavis Bioanalytical Instruments) using automated peptide synthesizer ResPep SL (Intavis Bioanalytical Instruments). All Fmoc-amino acids were purchased from Watanabe Chemical Industries and prepared at 0.5 M in N-methyl pyrrolidone (NMP, Wako Pure Chemical Industries). After synthesis, peptides were cleaved with (v/v/v) 92.5% TFA, 5% TIPS and 2.5% water for 2 h, precipitated using t-butyl-methyl-ether at -30º C, pelleted and resuspended in water before lyophilization (EYELA FDS-1000) overnight. All synthesized peptides' purity and sequence were then confirmed by LC-MS/MS using a Q-Exactive Plus Orbitrap hybrid mass spectrometer (Thermo Scientific) equipped with Ultimate 3000 nano-HPLC system (Dionex), HTC-PAL autosampler (CTC Analytics), and nanoelectrospray ion source.

358
359 **MT-dynamin binding assay**
360 Microtubule binding assay was performed using Microtubule Binding Protein Spin Down
361 Assay Kit (cat#BK029, Cytoskeletion Inc., Denver, CO, USA). Briefly, 20 µl of 5 mg/ml tubulin in
362 general tubulin buffer (GTB; 80 mM PIPES pH7.0, 2 mM $MgCl_2$, 0.5 mM EGTA) supplemented
363 with 1 mM GTP were polymerized by adding 2 µl of cushion buffer (80 mM PIPES pH7.0, 1 mM
364 $MgCl_2$, 1 mM EGTA, 60% glycerol), and incubated at 35°C for 20 min. Microtubules were
365 stabilized with 20 µM Taxol. Taxol-stabilized microtubules (2.5 µM) and dynamin 1 (1 µM) were
366 incubated in GTB with or without 1 mM peptide at room temperature for 30 min. After incubation,
367 the 50 µl of mixture was loaded on top of 100 µl cushion buffer supplemented with 20 µM Taxol,
368 and then centrifuged at 100,000 xg for 40 min at room temperature. After the ultracentrifugation,
369 50 µl of supernatant was taken and mixed with 10 µl of 5×sample buffer. The resultant pellet was
370 resuspended with 50 µl of 1×sample buffer. Twenty µl of each sample was analyzed by SDS-
371 PAGE and stained with SYPRO Orange. Protein bands were visualized using FLA-3000
372 (FUJIFILM Co.LTD, Tokyo, Japan).
373
374 **Immunocytochemical analysis**
375 The following primary antibodies were used: anti-β3-tubulin (Synaptic System, #302304),
376 anti-human Tau (BioLegend, #806501), anti-dynamin (Invitrogen, PA1-660). Secondary
377 antibodies were goat IgG conjugated with Alexa Fluor 488, 568, or 647 (Thermo Fisher
378 Scientific). Acute brainstem slices (175 µm in thickness, see below) were fixed with 4%
379 paraformaldehyde in PBS for 30 min at 37 ^{o}C and overnight at 4 ^{o}C. On the following day, slices
380 were rinsed three times in PBS, permeabilized in PBS containing 0.5% Triton X-100 (Tx-100;
381 Nacalai Tesque) for 30 min and blocked in PBS containing 3% bovine serum albumin (BSA;
382 Sigma-Aldrich) and 0.05% Tx-100 for 45 min. Slices were incubated overnight at 4 ^{o}C with
383 primary antibody diluted in PBS 0.05% Tx-100, 0.3% BSA. On the next day, slices were rinsed
384 three times with PBS containing 0.05% Tx-100 for 10 min and incubated with corresponding
385 secondary antibody diluted in PBS 0.05% Tx-100, 0.3% BSA for 1 h at room temperature (RT).
386 Slices were further rinsed three times in PBS 0.05% Tx-100 for 10 min and finally washed in PBS
387 for another 10 min. Finally, slices were mounted on glass slides (Matsunami) using liquid
388 mounting medium (Ibidi) and sealed using nail polish. Confocal images were acquired on laser
389 scanning microscopes (LSM780 or LSM900, Carl Zeiss) equipped with a Plan-apochromat 63x
390 oil-immersion objective (1.4 NA) and 488, 561, and 633 nm excitation laser lines. For quantifying
391 fluorescence intensity levels, the region of interest was delimited around calyceal terminals, and
392 background fluorescence was subtracted using ImageJ software.
393
394 **Purification of GST-proteins**
395 The cDNA encoding PH domain (521-618 amino acids) of human dynamin 1
396 (NM_004408.4) (75) were prepared by PCR and subcloned into the plasmid pGEX-6P vector.
397 The resulting plasmid was transformed into bacterial BL21(DE3) pLysS strain for protein
398 expression. The expression of GST-fusion proteins was induced by 0.1 mM isopropyl-1-thio-D-
399 galactopyranoside (IPTG) at 37°C for 3–6 h in LB media supplemented with 100 µg/ml ampicillin
400 at A_{600}=0.8. GST-fusion proteins were then purified as described(76). The nucleotide sequences
401 of the constructs using in this study were verified with DNA sequence analysis. All the purified
402 protein solutions (1–3 mg/ml) were stored at -80°C and thawed at 37°C before use.
403
404 **Microscopic observation of microtubule and GST-PH protein**
405 GST or GST-PH was labeled using HiLyte Fluor-555 labeling kit according to
406 manifacture's manual (cat#LK14, Dojindo Co. LTD, Kumamoto, Japan). HiLyte Fluor-555 labeled
407 GST or GST-PH was mixed with non-labelled each protein at the ratio of 1:1.2. Flutax1-stabilized
408 microtubules (4.1 µM) and fluorescent GST or GST-PH at 11 µM were mixed in GTB containing 2
409 µM Flutax1 at 37°C for 60 min. Eight µl of the mixture was spotted on the slide glass and
410 mounted with Fluoromount (cat#K024, Diagonistic BioSystems, CA, USA). Samples were
411 examined using a spinning disc confocal microscope system (X-Light Confocal Imager; CREST

412 OPTICS S.P.A., Rome, Italy) combined with an inverted microscope (IX-71; Olympus Optical Co.,
413 Ltd., Tokyo, Japan) and an iXon+ camera (Oxford Instruments, Oxfordshire, UK). The confocal
414 system was controlled by MetaMorph software (Molecular Devices, Sunnyvale, CA, USA). When
415 necessary, images were processed using Adobe Photoshop CS3 or Illustrator CS3 software. For
416 electron microscopic observation, samples were submitted to negative staining for imaging with a
417 transmission electron microscope (TEM) (H-7650, Hitachi High-Tech Corp., Tokyo, Japan) at 120
418 kV.
419
420 **Slice Electrophysiology**
421 After killing C57BL/6N mice of either sex (postnatal day 13-15) by decapitation under
422 isoflurane anesthesia, brainstems were isolated and transverse slices (175 μm thick) containing
423 the medial nucleus of the trapezoid body (MNTB) were cut using a vibratome (VT1200S, Leica) in
424 ice-cold artificial cerebrospinal fluid (aCSF, see below) with reduced Ca^{2+} (0.1 mM) and increased
425 Mg^{2+} (3 mM) concentrations or sucrose-based aCSF (NaCl was replaced to 300 mM sucrose,
426 concentrations of $CaCl_2$ and $MgCl_2$ was 0.1 mM and 6 mM, respectively). Slices were incubated
427 for 1h at 36-37 ^{o}C in standard aCSF containing (in mM); 125 NaCl, 2.5 KCl, 26 $NaHCO_3$, 1.25
428 $NaHPO_4$, 2 $CaCl_2$, 1 $MgCl_2$, 10 glucose, 3 myo-inositol, 2 sodium pyruvate, and 0.5 sodium
429 ascorbate (pH 7.4 when bubbled with 95 % O_2 and 5 % CO_2, 310-320 mOsm), and maintained
430 thereafter at room temperature (RT, 24-28 ^{o}C).
431 Whole-cell recordings were made using a patch-clamp amplifier (Multiclamp 700A,
432 Molecular Devices, USA for pair recordings and EPC-10 USB, HEKA Elektronik, Germany for
433 presynaptic capacitance measurements) from the calyx of Held presynaptic terminals and
434 postsynaptic MNTB principal neurons visually identified with a 60X or 40X water immersion
435 objective (LUMPlanFL, Olympus) attached to an upright microscope (Axioskop2, Carl Zeiss, or
436 BX51WI, Olympus, Japan). Data were acquired at a sampling rate of 50 kHz using pClamp (for
437 Multiclamp 700A) or Patchmaster software (for EPC-10 USB) after online filtering at 5 kHz. The
438 presynaptic pipette was pulled for the resistance of 7-10 MΩ and had a series resistance of 14-20
439 MΩ, which was compensated by 70 % for its final value to be 7 MΩ. Resistance of the
440 postsynaptic pipette was 5-7 MΩ, and its series resistance was 10-25 MΩ, which was
441 compensated by up to 75 % to a final value of 7 MΩ. The aCSF routinely contained picrotoxin
442 (10 μM) and strychnine hydrochloride (0.5 μM) to block $GABA_A$ receptors and glycine receptors,
443 respectively. Postsynaptic pipette solution contained (in mM): 130 CsCl, 5 EGTA, 1 $MgCl_2$, 5
444 QX314-Cl, 10 HEPES (adjusted to pH 7.3–7.4 with CsOH). The presynaptic pipette solution
445 contained (in mM); 105 K methanesulfonate, 30 KCl, 40 HEPES, 0.5 EGTA, 1 $MgCl_2$, 12
446 phosphocreatine (Na salt), 3 ATP (Mg salt), 0.3 GTP (Na salt) (pH 7.3-7.4 adjusted with KOH,
447 315-320 mOsm).
448 In simultaneous presynaptic and postsynaptic whole-cell recordings, postsynaptic MNTB
449 neurons were voltage-clamped at the holding potential of –70 mV, and EPSCs were evoked, at
450 0.1 Hz or 1 Hz, by action potentials elicited by a depolarizing current (1 ms) injected in calyceal
451 terminals. For intra-terminal loading of taxol (1 μM), it was diluted in presynaptic pipette solution
452 from 5 mM DMSO stock for final DMSO concentration to be 0.02%. Likewise, nocodazole (20 μM,
453 0.1% DMSO) was included in presynaptic pipette solution. Presynaptic pipette solutions in
454 nocodazole controls contained 0.1% DMSO. In simultaneous pre- and postsynaptic recordings,
455 WT h-tau, del-MTBD tau, taxol or synthetic peptides were loaded in calyceal terminals using the
456 pipette perfusion technique (42, 77). Briefly, a fine superfusion tube composed of plastic and
457 glass tubes was installed in a presynaptic patch pipette. After back-filling the tube with pipette
458 solutions containing proteins and/or peptides, it was inserted into a patch pipette with its tip 500-
459 600 μm behind the tip of presynaptic patch pipette. After recording baseline EPSCs, the tube
460 solution was delivered into presynaptic patch pipette with a positive pressure (8-10 psi) applied
461 using a pico-pump.
462 Membrane capacitance (C_m) measurements were made from calyx of Held presynaptic
463 terminals in the whole-cell configuration at RT (47, 49). Calyceal terminals were voltage-clamped
464 at a holding potential of -80 mV, and a sinusoidal voltage command (1 kHz, 60 mV in peak-to-
465 peak amplitude) was applied. To isolate presynaptic voltage-gated Ca^{2+} currents (I_{Ca}), the aCSF

contained 10 mM tetraethylammonium chloride, 0.5 mM 4-aminopyridine, 1 μM tetrodotoxin, 10 μM bicuculline methiodide and 0.5 μM strychnine hydrochloride. The presynaptic pipette solution contained (in mM): 125 Cs methanesulfonate, 30 CsCl, 10 HEPES, 0.5 EGTA, 12 disodium phosphocreatine, 3 MgATP, 1 $MgCl_2$, 0.3 Na_2GTP (pH 7.3 adjusted with CsOH, 315-320 mOsm). Tau or synthetic peptides were dissolved in pipette solution and backfilled into the pipette briefly after loading the tau-free pipette solution from the pipette tip. Care was taken to maintain series resistance < 16 MΩ to allow dialysis of the terminal with pipette solution. Recording pipette tips were coated with dental wax to minimize stray capacitance (4-5 pF). Single square pulse (-80 to 10 mV, 20 ms duration) was used to induce presynaptic I_{Ca}. In these experiments, exocytic capacitance change (ΔCm) represents ~ 5 times larger number of SVs (estimated from ΔCm divided by Cm of single SV) than that in the immediately releasable pool by presynaptic action potentials (estimated by the size of maximally evoked EPSCs divided by the size of miniature EPSCs). Membrane capacitance changes within 450 ms of square-pulse stimulation were excluded from analysis to avoid contamination by conductance-dependent capacitance artifacts (49). To avoid the influence of capacitance drift on baseline, we removed data when the baseline drift measured 0-10 s before stimulation was over 5 fFs^{-1}. When the drift was 1-5 fFs^{-1}, we subtracted a linear regression line of the baseline from the data for the baseline correction. The endocytic rate was calculated from the slope of the normalized C_m changes during the initial 10 s after the stimulation.

Data analysis and statistics

Data were analyzed using IGOR Pro 6 (WeveMatrics), Excel 2016 (Microsoft), and StatPlus (AnalystSoft Inc) and KaleidaGraph for Macintosh, version 4.1 (Synergy Software Inc., Essex Junction, VT, USA). All values are given as mean ± S.E.M. Differences were considered statistically significant at $p < 0.05$ in paired or unpaired *t*-tests, one-way *ANOVA* with Scheffe *post-hoc* test and repeated-measures two-way *ANOVA* with *post-hoc* Scheffe test.

Study approval

All experiments were carried out in accordance of the regulation and guidelines of Okinawa Institute of Science and Technology Graduate University (Approval number: 2021-347-00).

Acknowledgments

We thank Yasuo Ihara, Nobuyuki Nukina and Takeshi Sakaba for comments and Patrick Stoney for editing this paper. We also thank Shota Okuda and Mikako Matsubara for their contributions in the early stage of this study, and Satoko Wada-Kakuda for technical assistant with *in vitro* analysis of tau. This research was supported by funding from Okinawa Institute of Science and Technology and from Technology (OIST) and Core Research for the Evolutional Science and Technology of Japan Science and Technology Agency (CREST) to T.T., and by Scientific Research on Innovative Areas to T.M (Brain Protein Aging and Dementia Control 26117004).

References

1. K. R. Brunden, J. Q. Trojanowski, V. M. Lee, Advances in tau-focused drug discovery for Alzheimer's disease and related tauopathies. *Nat Rev Drug Discov* 8, 783-793 (2009).
2. V. M. Lee, K. R. Brunden, M. Hutton, J. Q. Trojanowski, Developing therapeutic approaches to tau, selected kinases, and related neuronal protein targets. *Cold Spring Harb Perspect Med* 1, a006437 (2011).

3. L. I. Binder, A. Frankfurter, L. I. Rebhun, The distribution of tau in the mammalian central nervous system. *J Cell Biol* 101, 1371-1378 (1985).
4. A. Kubo *et al.*, Distribution of endogenous normal tau in the mouse brain. *J Comp Neurol* 527, 985-998 (2019).
5. J. Biernat, N. Gustke, G. Drewes, E. M. Mandelkow, E. Mandelkow, Phosphorylation of Ser262 strongly reduces binding of tau to microtubules: distinction between PHF-like immunoreactivity and microtubule binding. *Neuron* 11, 153-163 (1993).
6. D. N. Drechsel, A. A. Hyman, M. H. Cobb, M. W. Kirschner, Modulation of the dynamic instability of tubulin assembly by the microtubule-associated protein tau. *Mol Biol Cell* 3, 1141-1154 (1992).
7. C. Ballatore, V. M. Lee, J. Q. Trojanowski, Tau-mediated neurodegeneration in Alzheimer's disease and related disorders. *Nat Rev Neurosci* 8, 663-672 (2007).
8. M. G. Spillantini, M. Goedert, Tau pathology and neurodegeneration. *Lancet Neurol* 12, 609-622 (2013).
9. S. G. Greenberg, P. Davies, A preparation of Alzheimer paired helical filaments that displays distinct tau proteins by polyacrylamide gel electrophoresis. *Proc Natl Acad Sci U S A* 87, 5827-5831 (1990).
10. I. Grundke-Iqbal *et al.*, Abnormal phosphorylation of the microtubule-associated protein tau (tau) in Alzheimer cytoskeletal pathology. *Proc Natl Acad Sci U S A* 83, 4913-4917 (1986).
11. H. Yoshida, Y. Ihara, Tau in paired helical filaments is functionally distinct from fetal tau: assembly incompetence of paired helical filament-tau. *J Neurochem* 61, 1183-1186 (1993).
12. M. Morris, S. Maeda, K. Vossel, L. Mucke, The many faces of tau. *Neuron* 70, 410-426 (2011).
13. J. Gotz, L. M. Ittner, M. Fandrich, N. Schonrock, Is tau aggregation toxic or protective: a sensible question in the absence of sensitive methods? *J Alzheimers Dis* 14, 423-429 (2008).
14. D. J. Koss *et al.*, Soluble pre-fibrillar tau and beta-amyloid species emerge in early human Alzheimer's disease and track disease progression and cognitive decline. *Acta Neuropathol* 132, 875-895 (2016).
15. A. Harada *et al.*, Altered microtubule organization in small-calibre axons of mice lacking tau protein. *Nature* 369, 488-491 (1994).
16. K. A. Vossel *et al.*, Tau reduction prevents Abeta-induced defects in axonal transport. *Science* 330, 198 (2010).
17. A. Yuan, A. Kumar, C. Peterhoff, K. Duff, R. A. Nixon, Axonal transport rates in vivo are unaffected by tau deletion or overexpression in mice. *J Neurosci* 28, 1682-1687 (2008).
18. L. M. Ittner *et al.*, Dendritic function of tau mediates amyloid-beta toxicity in Alzheimer's disease mouse models. *Cell* 142, 387-397 (2010).
19. E. D. Roberson *et al.*, Reducing endogenous tau ameliorates amyloid beta-induced deficits in an Alzheimer's disease mouse model. *Science* 316, 750-754 (2007).
20. J. A. Fein *et al.*, Co-localization of amyloid beta and tau pathology in Alzheimer's disease synaptosomes. *Am J Pathol* 172, 1683-1692 (2008).
21. H. C. Tai *et al.*, The synaptic accumulation of hyperphosphorylated tau oligomers in Alzheimer disease is associated with dysfunction of the ubiquitin-proteasome system. *Am J Pathol* 181, 1426-1435 (2012).
22. A. de Calignon *et al.*, Propagation of tau pathology in a model of early Alzheimer's disease. *Neuron* 73, 685-697 (2012).
23. L. Liu *et al.*, Trans-synaptic spread of tau pathology in vivo. *PLoS One* 7, e31302 (2012).
24. A. M. Pooler, E. C. Phillips, D. H. Lau, W. Noble, D. P. Hanger, Physiological release of endogenous tau is stimulated by neuronal activity. *EMBO Rep* 14, 389-394 (2013).
25. K. Yamada *et al.*, Neuronal activity regulates extracellular tau in vivo. *J Exp Med* 211, 387-393 (2014).

26. J. L. Guo, V. M. Lee, Seeding of normal Tau by pathological Tau conformers drives pathogenesis of Alzheimer-like tangles. *J Biol Chem* 286, 15317-15331 (2011).
27. M. Polydoro *et al.*, Soluble pathological tau in the entorhinal cortex leads to presynaptic deficits in an early Alzheimer's disease model. *Acta Neuropathol* 127, 257-270 (2014).
28. A. Sydow *et al.*, Tau-induced defects in synaptic plasticity, learning, and memory are reversible in transgenic mice after switching off the toxic Tau mutant. *J Neurosci* 31, 2511-2525 (2011).
29. Y. Yoshiyama *et al.*, Synapse loss and microglial activation precede tangles in a P301S tauopathy mouse model. *Neuron* 53, 337-351 (2007).
30. K. Santacruz *et al.*, Tau suppression in a neurodegenerative mouse model improves memory function. *Science* 309, 476-481 (2005).
31. J. McInnes *et al.*, Synaptogyrin-3 Mediates Presynaptic Dysfunction Induced by Tau. *Neuron* 97, 823-835 e828 (2018).
32. L. Zhou *et al.*, Tau association with synaptic vesicles causes presynaptic dysfunction. *Nat Commun* 8, 15295 (2017).
33. A. Ebneth *et al.*, Overexpression of tau protein inhibits kinesin-dependent trafficking of vesicles, mitochondria, and endoplasmic reticulum: implications for Alzheimer's disease. *J Cell Biol* 143, 777-794 (1998).
34. K. Shahpasand *et al.*, Regulation of mitochondrial transport and inter-microtubule spacing by tau phosphorylation at the sites hyperphosphorylated in Alzheimer's disease. *J Neurosci* 32, 2430-2441 (2012).
35. K. Stamer, R. Vogel, E. Thies, E. Mandelkow, E. M. Mandelkow, Tau blocks traffic of organelles, neurofilaments, and APP vesicles in neurons and enhances oxidative stress. *J Cell Biol* 156, 1051-1063 (2002).
36. E. Thies, E. M. Mandelkow, Missorting of tau in neurons causes degeneration of synapses that can be rescued by the kinase MARK2/Par-1. *J Neurosci* 27, 2896-2907 (2007).
37. A. Mudher *et al.*, GSK-3beta inhibition reverses axonal transport defects and behavioural phenotypes in Drosophila. *Mol Psychiatry* 9, 522-530 (2004).
38. L. Piriya Ananda Babu, H. Y. Wang, K. Eguchi, L. Guillaud, T. Takahashi, Microtubule and Actin Differentially Regulate Synaptic Vesicle Cycling to Maintain High-Frequency Neurotransmission. *J Neurosci* 40, 131-142 (2020).
39. H. S. Shpetner, R. B. Vallee, Identification of dynamin, a novel mechanochemical enzyme that mediates interactions between microtubules. *Cell* 59, 421-432 (1989).
40. C. Xie *et al.*, The homologous carboxyl-terminal domains of microtubule-associated protein 2 and TAU induce neuronal dysfunction and have differential fates in the evolution of neurofibrillary tangles. *PLoS One* 9, e89796 (2014).
41. S. Maeda *et al.*, Granular tau oligomers as intermediates of tau filaments. *Biochemistry* 46, 3856-3861 (2007).
42. T. Hori, Y. Takai, T. Takahashi, Presynaptic mechanism for phorbol ester-induced synaptic potentiation. *J Neurosci* 19, 7262-7267 (1999).
43. T. Takahashi, T. Hori, Y. Nakamura, T. Yamashita, Patch-Clamp Recording Method in Slices for Studying Presynaptic Mechanisms. 137-145 (2012).
44. M. Pusch, E. Neher, Rates of diffusional exchange between small cells and a measuring patch pipette. *Pflugers Arch* 411, 204-211 (1988).
45. S. Kar, J. Fan, M. J. Smith, M. Goedert, L. A. Amos, Repeat motifs of tau bind to the insides of microtubules in the absence of taxol. *EMBO J* 22, 70-77 (2003).
46. K. Eguchi *et al.*, Wild-Type Monomeric alpha-Synuclein Can Impair Vesicle Endocytosis and Synaptic Fidelity via Tubulin Polymerization at the Calyx of Held. *J Neurosci* 37, 6043-6052 (2017).
47. J. Y. Sun, L. G. Wu, Fast kinetics of exocytosis revealed by simultaneous measurements of presynaptic capacitance and postsynaptic currents at a central synapse. *Neuron* 30, 171-182 (2001).

48. H. Y. Wang, K. Eguchi, T. Yamashita, T. Takahashi, Frequency-Dependent Block of Excitatory Neurotransmission by Isoflurane via Dual Presynaptic Mechanisms. *J Neurosci* 40, 4103-4115 (2020).
49. T. Yamashita, T. Hige, T. Takahashi, Vesicle endocytosis requires dynamin-dependent GTP hydrolysis at a fast CNS synapse. *Science* 307, 124-127 (2005).
50. J. E. Hinshaw, S. L. Schmid, Dynamin self-assembles into rings suggesting a mechanism for coated vesicle budding. *Nature* 374, 190-192 (1995).
51. A. Raimondi *et al.*, Overlapping role of dynamin isoforms in synaptic vesicle endocytosis. *Neuron* 70, 1100-1114 (2011).
52. K. Takei, P. S. McPherson, S. L. Schmid, P. De Camilli, Tubular membrane invaginations coated by dynamin rings are induced by GTP-gamma S in nerve terminals. *Nature* 374, 186-190 (1995).
53. F. Bartolini, G. G. Gundersen, Formins and microtubules. *Biochim Biophys Acta* 1803, 164-173 (2010).
54. T. Sakaba *et al.*, Fast neurotransmitter release regulated by the endocytic scaffold intersectin. *Proc Natl Acad Sci U S A* 110, 8266-8271 (2013).
55. T. Soykan *et al.*, Synaptic Vesicle Endocytosis Occurs on Multiple Timescales and Is Mediated by Formin-Dependent Actin Assembly. *Neuron* 93, 854-866 e854 (2017).
56. K. R. Schuske *et al.*, Endophilin is required for synaptic vesicle endocytosis by localizing synaptojanin. *Neuron* 40, 749-762 (2003).
57. S. Watanabe *et al.*, Synaptojanin and Endophilin Mediate Neck Formation during Ultrafast Endocytosis. *Neuron* 98, 1184-1197 e1186 (2018).
58. C. Takami, K. Eguchi, T. Hori, T. Takahashi, Impact of vesicular glutamate leakage on synaptic transmission at the calyx of Held. *J Physiol* 595, 1263-1271 (2017).
59. L. Kong *et al.*, Cryo-EM of the dynamin polymer assembled on lipid membrane. *Nature* 560, 258-262 (2018).
60. T. M. La *et al.*, Dynamin 1 is important for microtubule organization and stabilization in glomerular podocytes. *FASEB J* 34, 16449-16463 (2020).
61. P. Zhang, J. E. Hinshaw, Three-dimensional reconstruction of dynamin in the constricted state. *Nat Cell Biol* 3, 922-926 (2001).
62. D. G. Drubin, M. W. Kirschner, Tau protein function in living cells. *J Cell Biol* 103, 2739-2746 (1986).
63. O. A. Shemesh, H. Erez, I. Ginzburg, M. E. Spira, Tau-induced traffic jams reflect organelles accumulation at points of microtubule polar mismatching. *Traffic* 9, 458-471 (2008).
64. F. Liu *et al.*, Site-specific effects of tau phosphorylation on its microtubule assembly activity and self-aggregation. *Eur J Neurosci* 26, 3429-3436 (2007).
65. S. Khatoon, I. Grundke-Iqbal, K. Iqbal, Brain levels of microtubule-associated protein tau are elevated in Alzheimer's disease: a radioimmuno-slot-blot assay for nanograms of the protein. *J Neurochem* 59, 750-753 (1992).
66. M. Goedert, B. Falcon, F. Clavaguera, M. Tolnay, Prion-like mechanisms in the pathogenesis of tauopathies and synucleinopathies. *Curr Neurol Neurosci Rep* 14, 495 (2014).
67. K. Maeda, T. Nakata, Y. Noda, R. Sato-Yoshitake, N. Hirokawa, Interaction of dynamin with microtubules: its structure and GTPase activity investigated by using highly purified dynamin. *Mol Biol Cell* 3, 1181-1194 (1992).
68. H. S. Shpetner, R. B. Vallee, Dynamin is a GTPase stimulated to high levels of activity by microtubules. *Nature* 355, 733-735 (1992).
69. K. Tanabe, K. Takei, Dynamic instability of microtubules requires dynamin 2 and is impaired in a Charcot-Marie-Tooth mutant. *J Cell Biol* 185, 939-948 (2009).
70. T. A. Fulga *et al.*, Abnormal bundling and accumulation of F-actin mediates tau-induced neuronal degeneration in vivo. *Nat Cell Biol* 9, 139-148 (2007).
71. B. Roger, J. Al-Bassam, L. Dehmelt, R. A. Milligan, S. Halpain, MAP2c, but not tau, binds and bundles F-actin via its microtubule binding domain. *Curr Biol* 14, 363-371 (2004).

72. T. Guo, W. Noble, D. P. Hanger, Roles of tau protein in health and disease. *Acta Neuropathol* 133, 665-704 (2017).
73. M. Hasegawa, M. J. Smith, M. Goedert, Tau proteins with FTDP-17 mutations have a reduced ability to promote microtubule assembly. *FEBS Lett* 437, 207-210 (1998).
74. H. Yamada *et al.*, Stabilization of actin bundles by a dynamin 1/cortactin ring complex is necessary for growth cone filopodia. *J Neurosci* 33, 4514-4526 (2013).
75. C. Gu *et al.*, Direct dynamin-actin interactions regulate the actin cytoskeleton. *EMBO J* 29, 3593-3606 (2010).
76. V. I. Slepnev, G. C. Ochoa, M. H. Butler, P. De Camilli, Tandem arrangement of the clathrin and AP-2 binding domains in amphiphysin 1 and disruption of clathrin coat function by amphiphysin fragments comprising these sites. *J Biol Chem* 275, 17583-17589 (2000).
77. T. Hori, T. Takahashi, Kinetics of synaptic vesicle refilling with neurotransmitter glutamate. *Neuron* 76, 511-517 (2012).

692
693
694 **Figures and Tables**

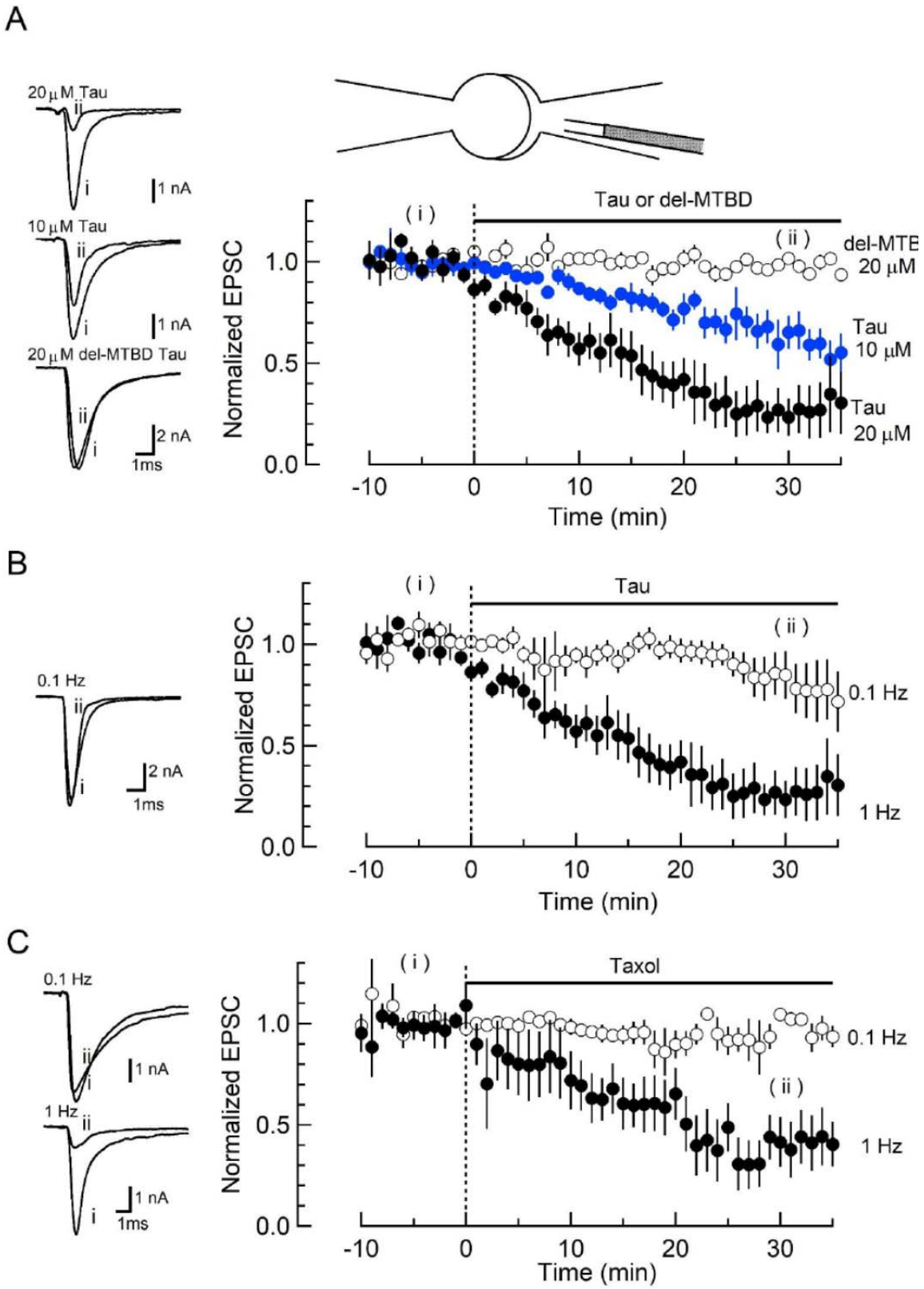
A
20 μM Tau
ii
i
1 nA
10 μM Tau
ii
i
1 nA
20 μM del-MTBD Tau
ii
i
2 nA
1ms
Tau or del-MTBD
(i)
(ii)
del-MTB
20 μM
Tau
10 μM
Tau
20 μM
Normalized EPSC
1.0
0.5
0.0
-10
0
10
20
30
Time (min)
B
0.1 Hz
ii
i
2 nA
1ms
Tau
(i)
(ii)
0.1 Hz
1 Hz
Normalized EPSC
1.0
0.5
0.0
-10
0
10
20
30
Time (min)
C
0.1 Hz
ii
i
1 nA
1 Hz
ii
i
1 nA
1ms
Taxol
(i)
(ii)
0.1 Hz
1 Hz
Normalized EPSC
1.0
0.5
0.0
-10
0
10
20
30
Time (min)

695

Figure 1. WT h-tau loaded in presynaptic terminals inhibited excitatory synaptic transmission (A) In simultaneous pre- and postsynaptic whole-cell recordings, intra-terminal infusion of WT h-tau at 10 μM (blue filled circles) or 20 μM (black filled circles), from a tube in a presynaptic patch pipette (top illustration), caused a concentration-dependent rundown of EPSCs evoked by presynaptic action potentials at 1 Hz. In the time plots, EPSC amplitudes averaged from 60 events are sampled for data points and normalized to the mean amplitude of baseline EPSCs before h-tau infusion. Sample records of EPSCs 5 min before (i) and 30 min after (ii) tau infusion are superimposed and shown on the left panels. The EPSC amplitude remaining 30 min after infusion was 23 ± 9 % and 65 ± 5 %, respectively for 10 μM and 20 μM h-tau (means and SEMs, 6 synapses from 6 slices, $p < 0.01$ in paired t-test between before and after h-tau infusion). Infusion of MT-binding site-deleted h-tau mutant (del-MTBD, 20 μM, Supplemental Figure S1A) had no effect on the EPSC amplitude (open circles, sample EPSC traces shown on the left bottom panel). (B) The amplitude of EPSCs evoked at 0.1 Hz remained unchanged after h-tau infusion (85 % ± 12 %, 5 synapses from 5 slices, $p = 0.22$ in paired t-test). Sample records of EPSCs before (i) and 30 min after (ii) h-tau infusion at 0.1 Hz are superimposed on the left panel. (C) Taxol (1 μM) caused activity-dependent rundown of EPSC amplitude to 41.4 ± 12 % at 1 Hz ($p < 0.01$, 5 synapses from 5 slices), but remained unchanged when stimulated at 0.1 Hz (105 ± 3.0 %, open circles, 4 synapses from 4 slices). Sample records of EPSCS at 0.1 Hz and 1 Hz are superimposed on the left panels.

Figure 1–source data 1. WT h-tau loaded in presynaptic terminals inhibited excitatory synaptic transmission

Figure 1 –figure supplement 1. Tubulin polymerization assay for purified 0N4R WT h-tau and MT-binding region-deleted mutant (A) *Left panel*, schematic drawings of WT 0N4R h-tau (a) and h-tau deletion mutant lacking the MT-binding region (del-MTBD, b). *Right panel*, purified recombinant WT 0N4R h-tau (a) and del-MTBD (b) in SDS-PAGE with molecular markers (M) on the left lane. (B) *In vitro* tubulin polymerization assay, showing MT assembly by WT h-tau (10 μM, open circles) or taxol (1 μM, filled triangles), but not by del-MTBD (10 μM, open squares) or tubulin alone (filled circles). Data points and bars represent means and SEMs (n =3).

Figure 1 –figure supplement 1 –source data 1. Raw SDS-PAGE gel data from Figure 1 figure supplement 1 A

Figure 1 –figure supplement 1 –source data 2. Data from Figure 1 figure supplement 1 B

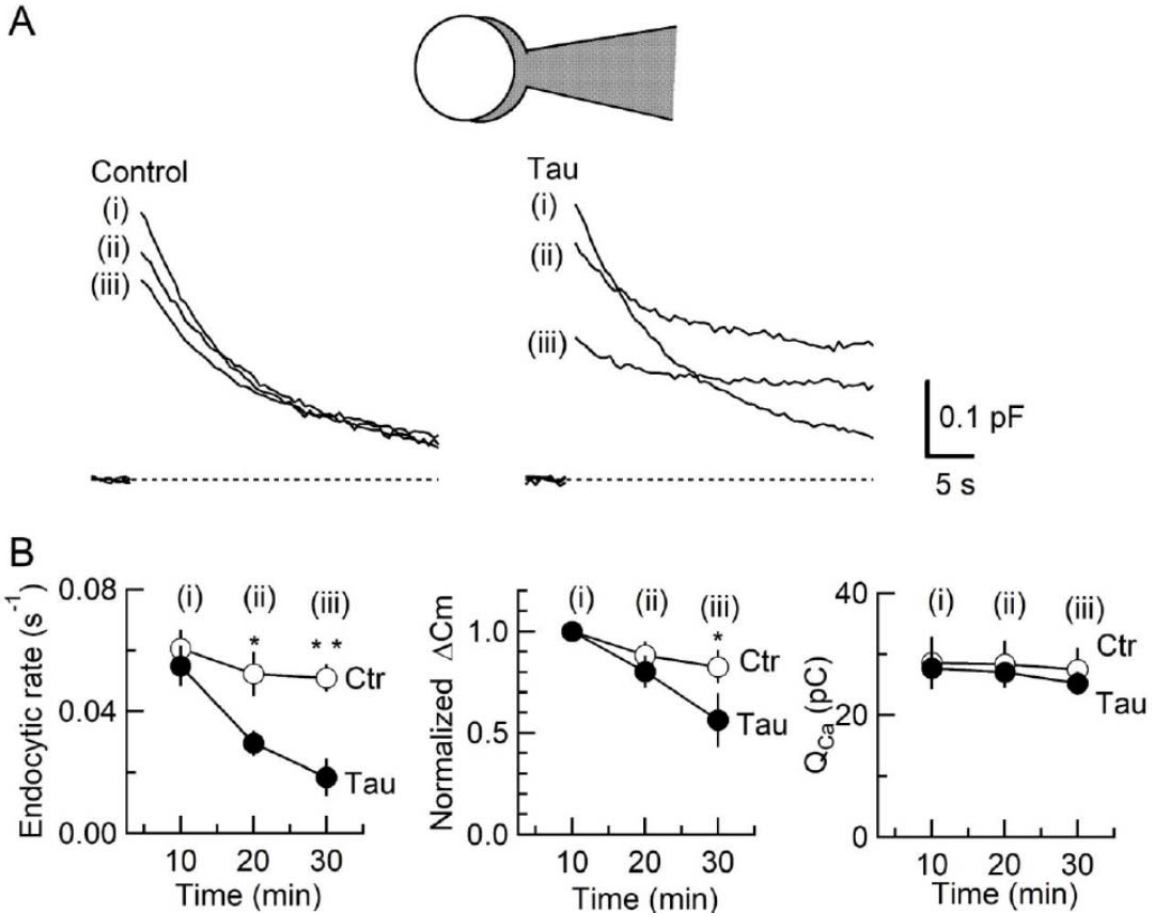

Figure 2. Inhibition of SV endocytosis is the primary effect of WT h-tau loading (A) Exo-endocytic membrane capacitance changes in presynaptic terminals without (Control) or after direct loading of WT h-tau (20 μM; Tau). WT h-tau was directly loaded by diffusion into a terminal from a whole-cell patch pipette (illustration). Capacitance traces were sampled from (i) 10, (ii) 20 and (iii) 30 min after patch membrane rupture (superimposed). *Left panel*, non-loading control. *Right panel*, WT h-tau-loaded terminal. Capacitance changes were evoked every 2 min by Ca^{2+} currents induced by a 20-ms depolarizing pulse (not shown). (B) Time plots of endocytic rate (left panel), exocytic magnitude (middle panel) and presynaptic Ca^{2+} current charge (right panel). Data points represent averaged values from 5 events from 4 min before and 4 min after the time points. In calyceal terminals, 20 min after patch membrane rupture with a pipette containing WT h-tau (filled circles; Tau), endocytic rate was significantly prolonged ($p < 0.05$ compared to controls, open circles, repeated-measures two-way *ANOVA* with *post-hoc* Scheffe test, n = 5 from 5 slices), whereas exocytic magnitude remained similar to controls ($p = 0.45$). 30 min after rupture, endocytic rate was further prolonged ($p < 0.01$) and exocytic magnitude became significantly less than controls ($p < 0.05$). Ca^{2+} current charge (Q_{Ca}) remained unchanged throughout recording.

Figure 2–source data 1. Inhibition of SV endocytosis is the primary effect of WT h-tau loading

752

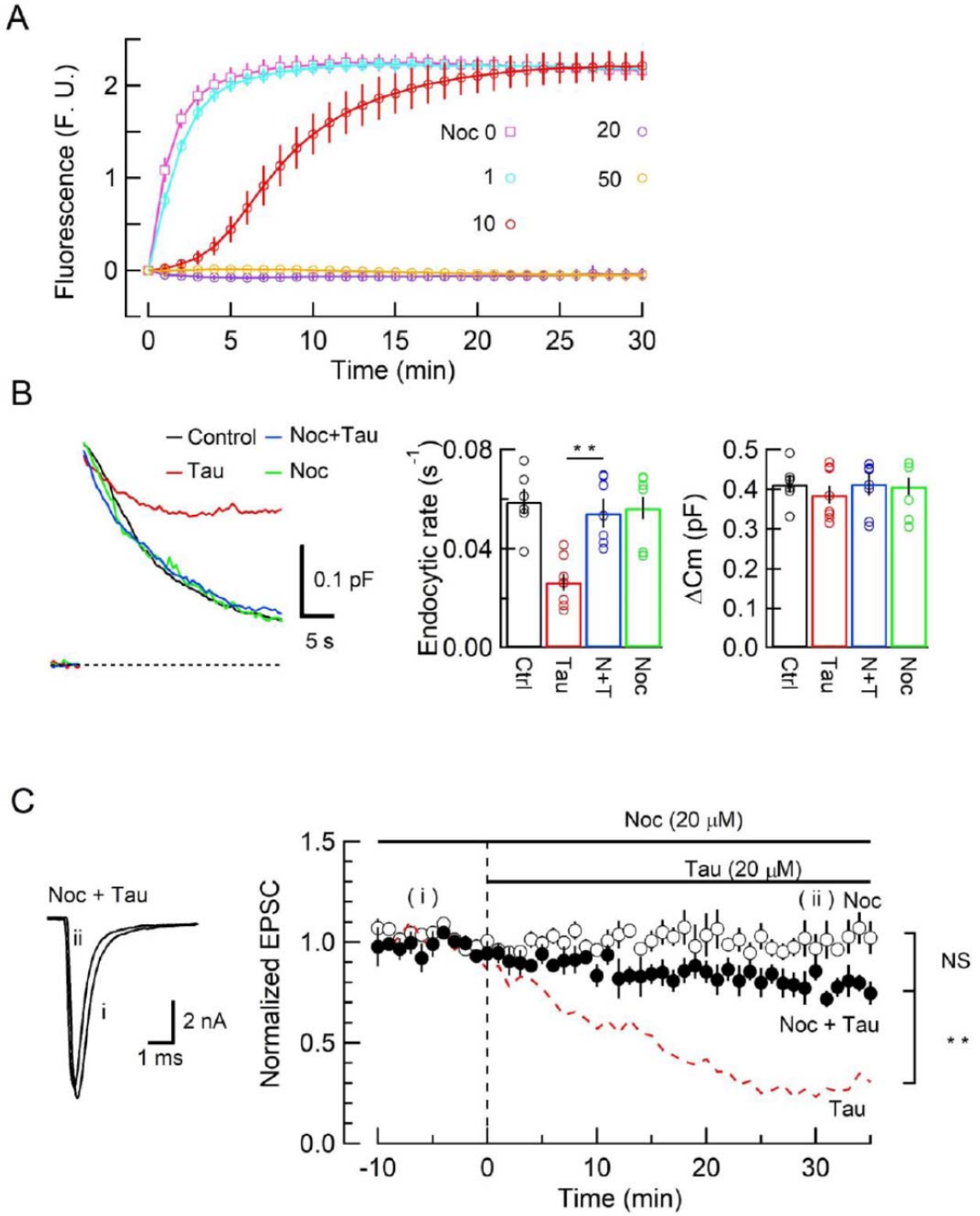

753
754 **Figure 3. The MT assembly blocker nocodazole prevented tau-induced block of SV**
755 **endocytosis and EPSC rundown** (A) Concentration-dependent inhibitory effects of nocodazole
756 on MT assembly in tubulin polymerization assay. MT assembly by 0N4R h-tau (20 μM) in the
757 absence (pink symbols and a fitting line) or presence of nocodazole at 1 μM (blue), 10 μM (red),
758 20 μM (purple) and 50 μM (orange). Data points and error bars in all graphs represent means and
759 SEMs (n = 3). (B) Nocodazole prevented h-tau-induced block of SV endocytosis. Presynaptic

membrane capacitance changes (superimposed traces) 25 min after loading h-tau alone (20 μM, red trace), h-tau and nocodazole (20 μM, blue), nocodazole alone (20 μM, green) and controls with no loading (black). Bar graphs indicate endocytic rates in non-loading controls (Ctr, black, 6 terminals from 6 slices), h-tau loaded terminals (Tau, red, 8 terminals from 8 slices), co-loading of nocodazole with h-tau (N+T, blue, 7 terminals from 7 slices) and nocodazole alone (Noc, green, 8 terminals from 8 slices). Nocodazole co-loading fully prevented endocytic block by h-tau ($p < 0.01$, between Tau and N-T) to control level (one-way ANOVA with Scheffe *post hoc* test).

(C) Nocodazole prevented EPSC rundown caused by WT h-tau. Nocodazole (20 μM) co-loaded with WT h-tau (20 μM) prevented EPSC rundown (filled circles, 4 synapses from 4 slices, $p < 0.01$, unpaired t-test). Data of WT h-tau effect on EPSCs (Figure 1A) is shown as a red dashed line for comparison. Nocodazole alone (20 μM) had no effect on EPSC amplitude throughout (open circles, 4 synapses from 4 slices).

Figure 3–source data 1. The MT assembly blocker nocodazole prevented tau-induced block of SV endocytosis and EPSC rundown

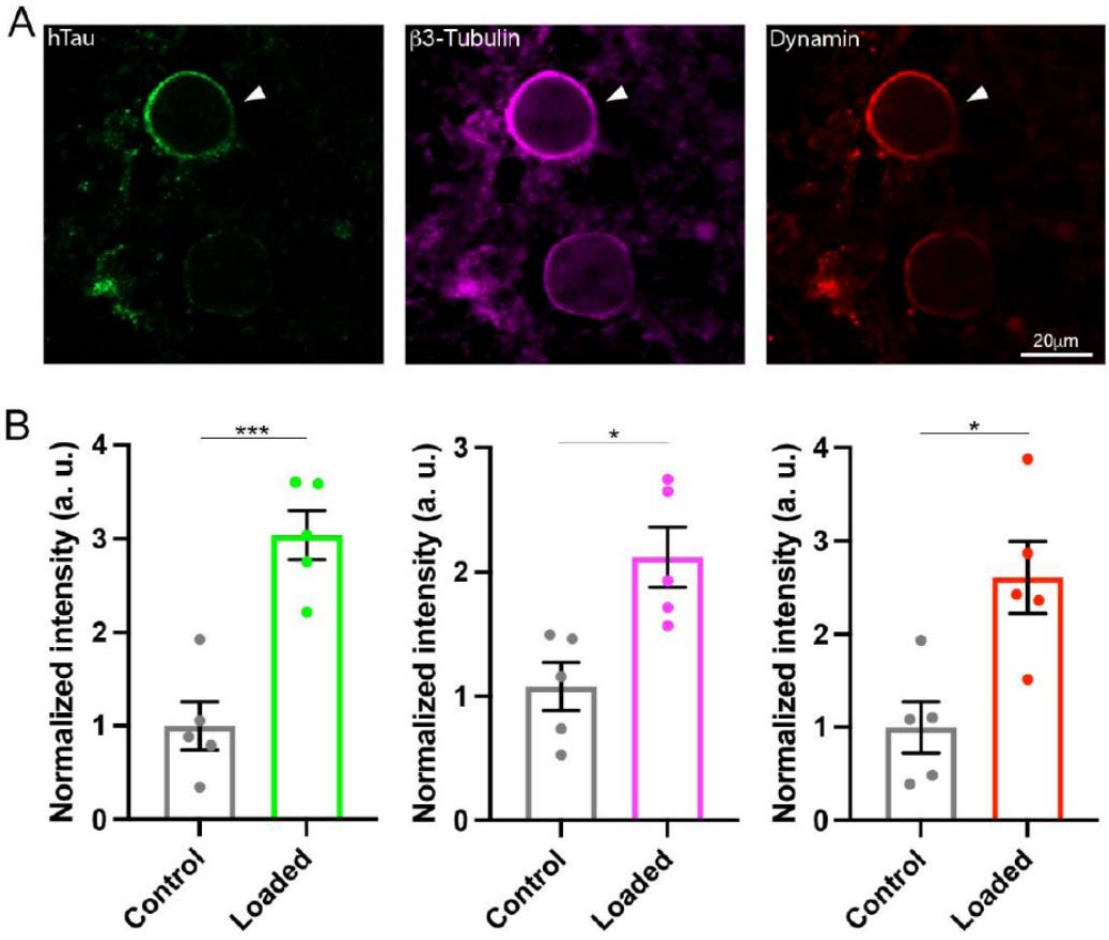
A
hTau
β3-Tubulin
Dynamin
20μm
B
Normalized intensity (a. u.)
***
*
*
Control
Loaded

776
777

Figure 4. WT h-tau assembled MTs and increased bound-form dynamins in calyceal terminals (A) Immunofluorescence images of brainstem slices showing loaded WT h-tau (green, left, arrowhead) labeled with anti h-tau/AlexaFluor-488 antibodies (green, left panel), newly assembled MTs labeled with anti β3-tubulin/AlexaFluor-647 antibodies (magenda, middle) and increased bound-form dynamin labeled with anti dynamin1/AlexaFluor-568 antibodies (red, right panel). (B) Bar graphs showing immunofluorescence intensities of h-tau (green), β3-tubulin (magenda) and dynamin (red) relative to controls with no loading (black bars). WT h-tau loading significantly increased β3-tubulin ($p = 0.0105$) and dynamin1 ($p = 0.0109$) intensity in terminals compared to control terminals without WT h-tau loading ($n = 5$ terminals from 5 slices for each data set, two-tailed unpaired t-test with Welch's correction; * $p < 0.05$, *** $p < 0.001$).

Figure 4 –source data 1. Raw immunofluorescence images from Figure 4A

Figure 4 –source data 2. Data from Figure 4B

Figure 4 –figure supplement 1. Super-resolution imaging of h-tau-infused calyx of Held. (A) Low magnification image of the terminal showing h-tau (green), β3-tubulin (blue) and dynamin-1 (red). Images were acquired on LSM900 with Airyscan 2 super-resolution module followed by 3D deconvolution. Scale bar, 5 μm. Corresponding 3D surface rendering image is shown on the right panel. (B) Expanded views of the delineated area in panel A, showing close localization of dynamin 1 with MT bundles in the presynaptic terminal infused with h-tau, and corresponding 3D surface rendering image (bottom panel). Scale bar, 1 μm.

Figure 4 –figure supplement 1–source data 1. Raw images from Figure 4 –figure supplement 1

Figure 4 –figure supplement 2. Effects of a formin mDia inhibitor on SV endocytosis and tau infusion on the quantal EPSCs. (A) Formin mDia inhibitor SMIFH2 (50μM) has no significant effect on SV endocytic rate (middle panel bar graphs, $p =0.45$, $n = 4$) or exocytic magnitude (right panel bar graphs, $p = 0.88$, $n = 4$) at the calyx of Held of post-hearing mice (P13-14). Sample traces of capacitance changes evoked by a 20 ms pule with (red) or without (black) SMIFH2 are superimposed in the left panel. (B) Intra-terminal h-tau infusion had no effect on the mean amplitude ($p = 0.08$, t-test, $n = 4$) or frequency ($p = 0.07$, t-test, $n = 4$) of spontaneous miniature EPSCs. Left panel, sample trace 5 min before (control, upper trace) and 30 min after tau infusion (lower trace) in a simultaneous pre- and postsynaptic recording experiment.

Figure 4 –figure supplement 2–source data 1. Data from Figure 4 –figure supplement 2

A

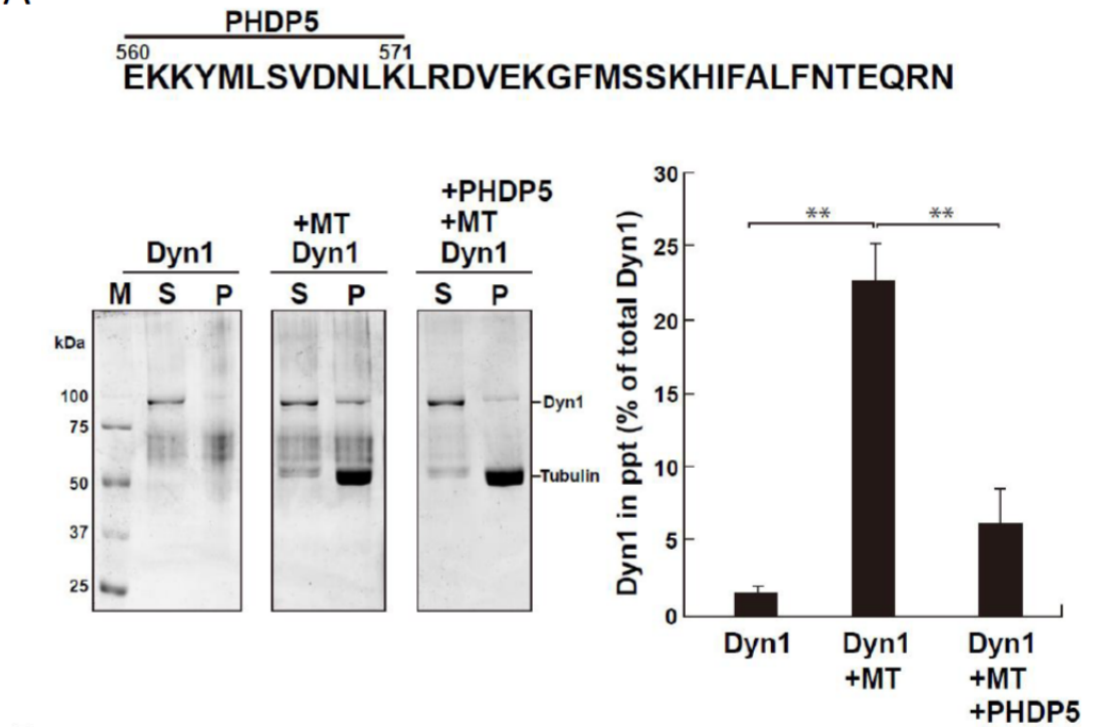
PHDP5
560
571
EKKYMLSVDNLKLRDVEKGFMSSKHIFALFNTEQRN
Dyn1
+MT Dyn1
+PHDP5 +MT Dyn1
M S P
S P
S P
kDa
100
75
50
37
25
Dyn1
Tubulin
Dyn1 in ppt (% of total Dyn1)
**
**
Dyn1
Dyn1 +MT
Dyn1 +MT +PHDP5

B

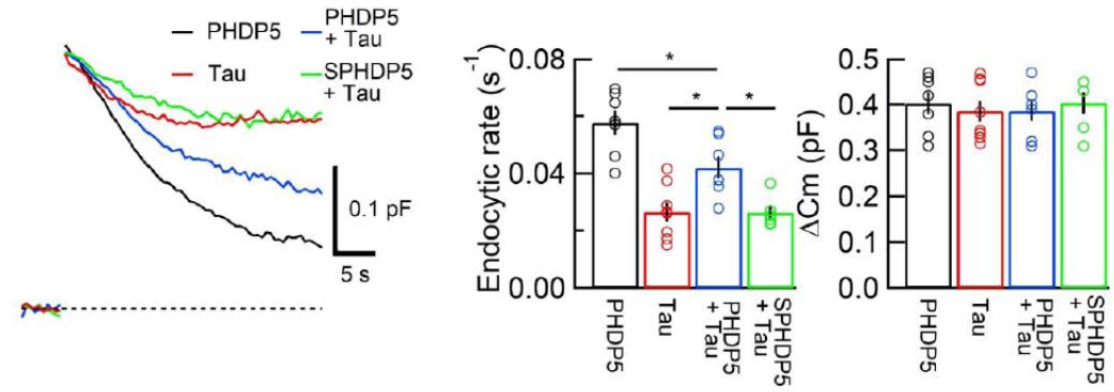
PHDP5
PHDP5 + Tau
Tau
SPHDP5 + Tau
0.1 pF
5 s
Endocytic rate (s-1)
0.08
0.04
0.00
*
*
*
ΔCm (pF)
0.5
0.4
0.3
0.2
0.1
0.0
PHDP5
Tau
PHDP5 + Tau
SPHDP5 + Tau

C

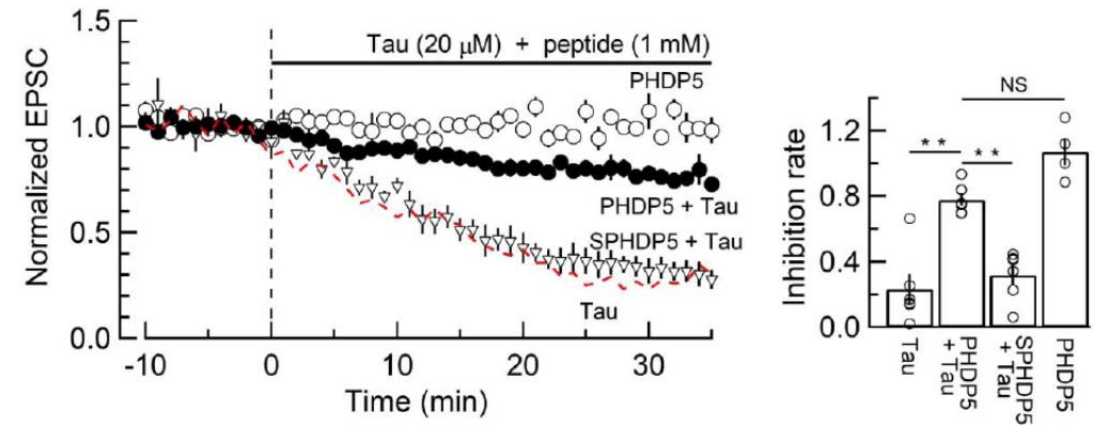
Normalized EPSC
1.5
1.0
0.5
0.0
Tau (20 μM) + peptide (1 mM)
PHDP5
PHDP5 + Tau
SPHDP5 + Tau
Tau
-10
0
10
20
30
Time (min)
Inhibition rate
NS
**
**
1.2
0.8
0.4
0.0
Tau
PHDP5 + Tau
SPHDP5 + Tau
PHDP5

811

Figure 5. dynamin 1 PH domain peptide inhibited MT-dynamin 1 binding and prevented endocytic slowing and EPSC rundown caused by WT h-tau (A) *Top*, Partial amino acid sequence of PH domain of mouse dynamin 1 indicating the sequence of the synthetic dodecapeptide PHDP5 (560-571). *Left,* SDS-PAGE of MT-dynamin 1 binding assay. S, supernatant; P, precipitates. Dyn1, dynamin 1. *Right*, quantification of MT-dynamin 1 interaction. The bars indicate the percentage of dynamin 1 found in precipitates relative to total amount. PHDP5 significantly inhibited MT-dynamin 1 interaction (**<0.01, n = 3). (B) Presynaptic membrane capacitance records (superimposed) after loading h-tau alone (20 μM, red trace, taken from Figure 4B), h-tau co-loaded with DPHP5 (0.25 mM, blue) or scrambled DPHP5 (SDPHP5, green). DPHP5 alone (0.25 mM, black trace, 7 terminals from 7 slices) had no effect on capacitance changes compared to non-loading terminal controls (taken from Figure 3B). Bar graphs of endocytic rates (middle panel) indicate significant difference ($p < 0.05$, 7 terminals from 7 slices) between tau (red bar, 8 terminals from 8 slices) and DPHP5+tau (blue, 7 terminals from 7 slices) as well as between SDPHP5 + tau (blue) and DPHP5+ tau (green, n = 6 terminals from 6 slices). The magnitudes of exocytic capacitance changes were not significantly different between the groups, recorded 25 min after rupture). (C) DPHP5 attenuated h-tau induced EPSC rundown. The EPSC rundown after h-tau infusion (20 μM, red dashed line; data taken from Fig 1A) was attenuated by DPHP5 (1 mM) co-loaded with h-tau (filled circles) but not by scrambled DPHP5 peptide (SDPHP5, open triangles, 1 mM). DPHP5 alone (1 mM, open circles) had no effect on EPSC amplitude throughout. Bar graphs indicate EPSC amplitude (normalized to that before infusion) 30 min after infusion. Significant difference ($p < 0.01$) between tau and tau + DPHP5, between tau + DPHP5 and tau + SDPHP5. The difference between DPHP5 alone and DPHP5 + tau was not significant ($p = 0.09$), indicating the partial antagonistic effect of DPHP5 against h-tau-induced EPSC rundown.

Figure 5 –source data 1. Data from Figure 5A

Figure 5 –source data 2. Data from Figure 5B and C

Figure 5 –source data 3. Images from Figure 5A

Figure 5 –figure supplement 1. PHDP5 strongly inhibited dynamin 1 binding to microtubules (A) Peptide sequences in mouse dynamin 1 used in the DN peptide screening. In total, 24 peptides covering the PH domain and the proline-rich domain were synthesized. (B) SDS-PAGE of the microtubule binding assay, showing that PHDP5 strongly inhibits the MT-dynamin 1 binding ("+Pep5" in the top right panel). Since 5 peptides (peptide6, peptide8, peptide9, peptide10, peptide11) were insoluble in water or dimethyl sulfoxide, their effects were not tested. (C) Effects of the synthetic peptides at 1 mM on MT-dynamin1 binding. Bar graphs indicate the percentage of dynamin 1 found in precipitates relative to total amount.

Figure 5 –figure supplement 1–source data 1. Images from Figure 5 –figure supplement 1

Figure 5 –figure supplement 1–source data 2. Data from Figure 5 –figure supplement 1

Figure 5 –figure supplement 2. PH domain of dynamin 1 directly binds to microtubules. (A) *Left panels,* GST-PH labelled with HiLyte Fluor-555 (red, GST-PH) highly localized with fluorescent microtubules (green, MT). Scale bar, 20 μm. *Right panels*, GST without PH did not co-localize with MTs. (B) Electron micrograph of negatively-stained MTs (*upper left panel*), MTs plus GST-PH (*upper middle panel*), GST-PH alone (*upper right panel*), MTs plus GST (*lower left* panel), GST alone (*lower right panel*). GST-PH binds and crosslinks MTs. GST-PH forms larger complexes compared to GST. Scale Bar, 200 nm.

Figure 5 –figure supplement 2–source data 1. Images from Figure 5 –figure supplement 2

A

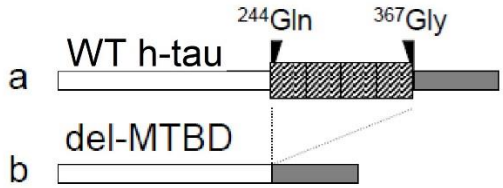
244Gln
367Gly
a
WT h-tau
b
del-MTBD

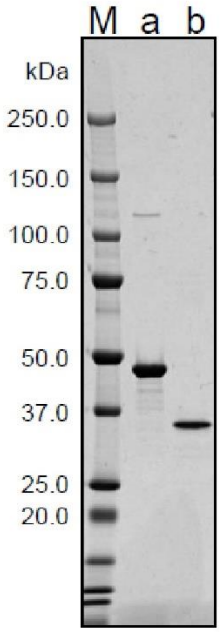
M a b
kDa
250.0
150.0
100.0
75.0
50.0
37.0
25.0
20.0

B

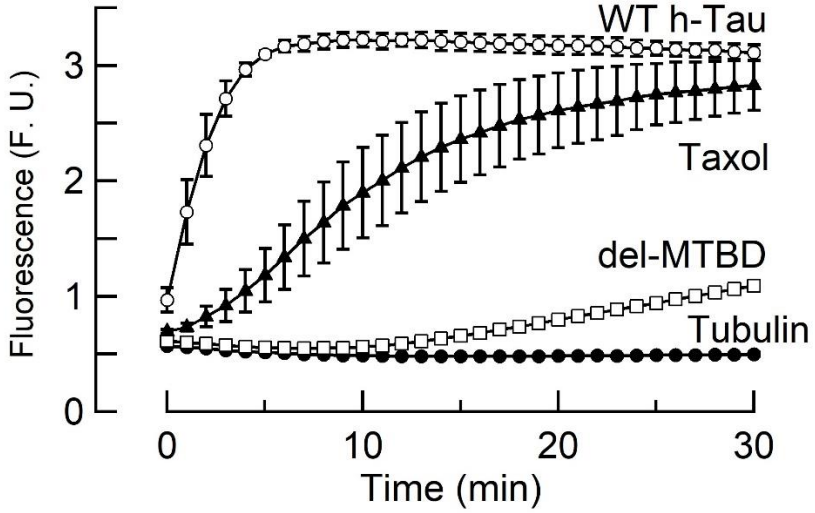
WT h-Tau
Taxol
del-MTBD
Tubulin
Fluorescence (F. U.)
0
1
2
3
0
10
20
30
Time (min)

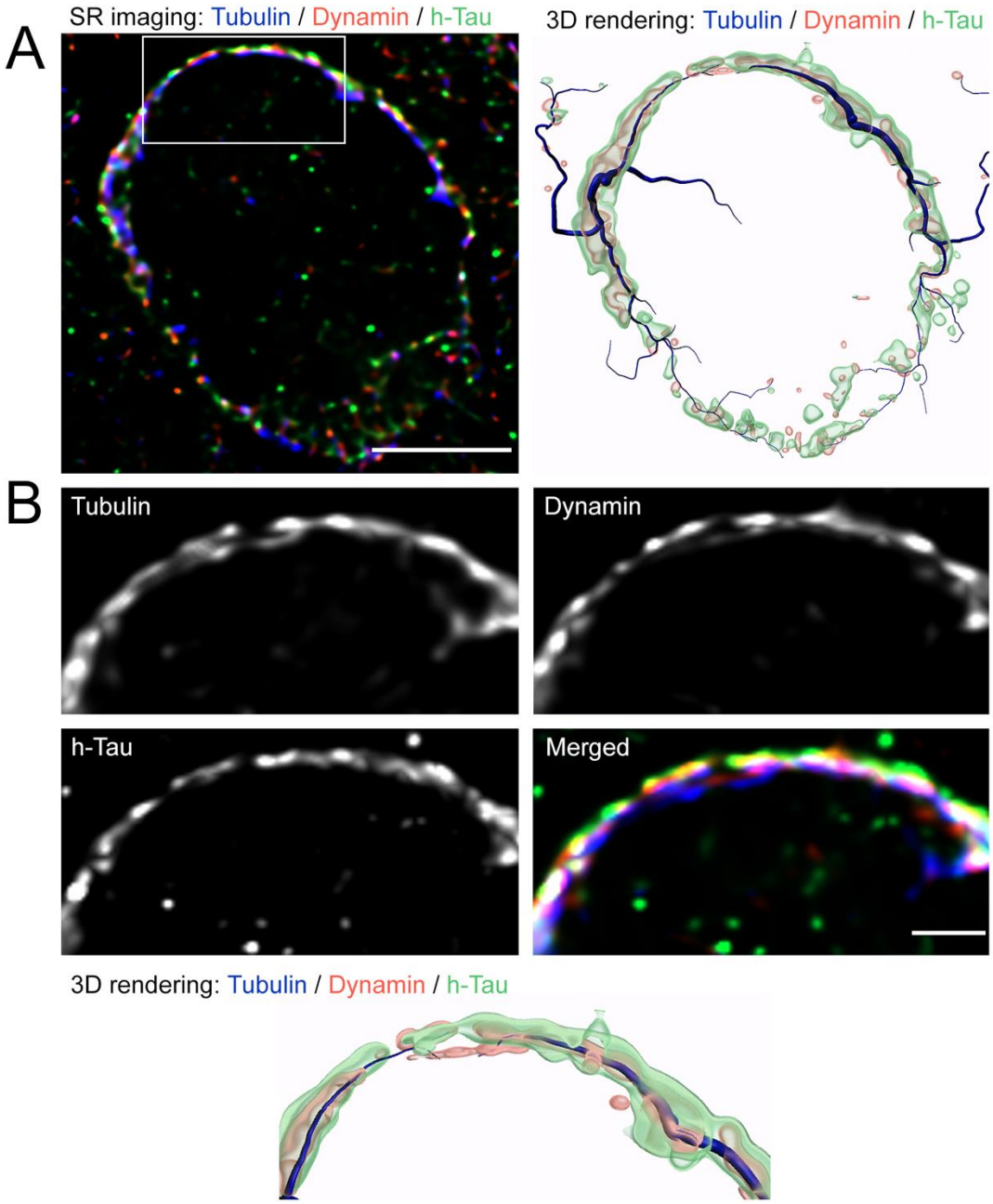
A
SR imaging: Tubulin / Dynamin / h-Tau
3D rendering: Tubulin / Dynamin / h-Tau
B
Tubulin
Dynamin
h-Tau
Merged
3D rendering: Tubulin / Dynamin / h-Tau

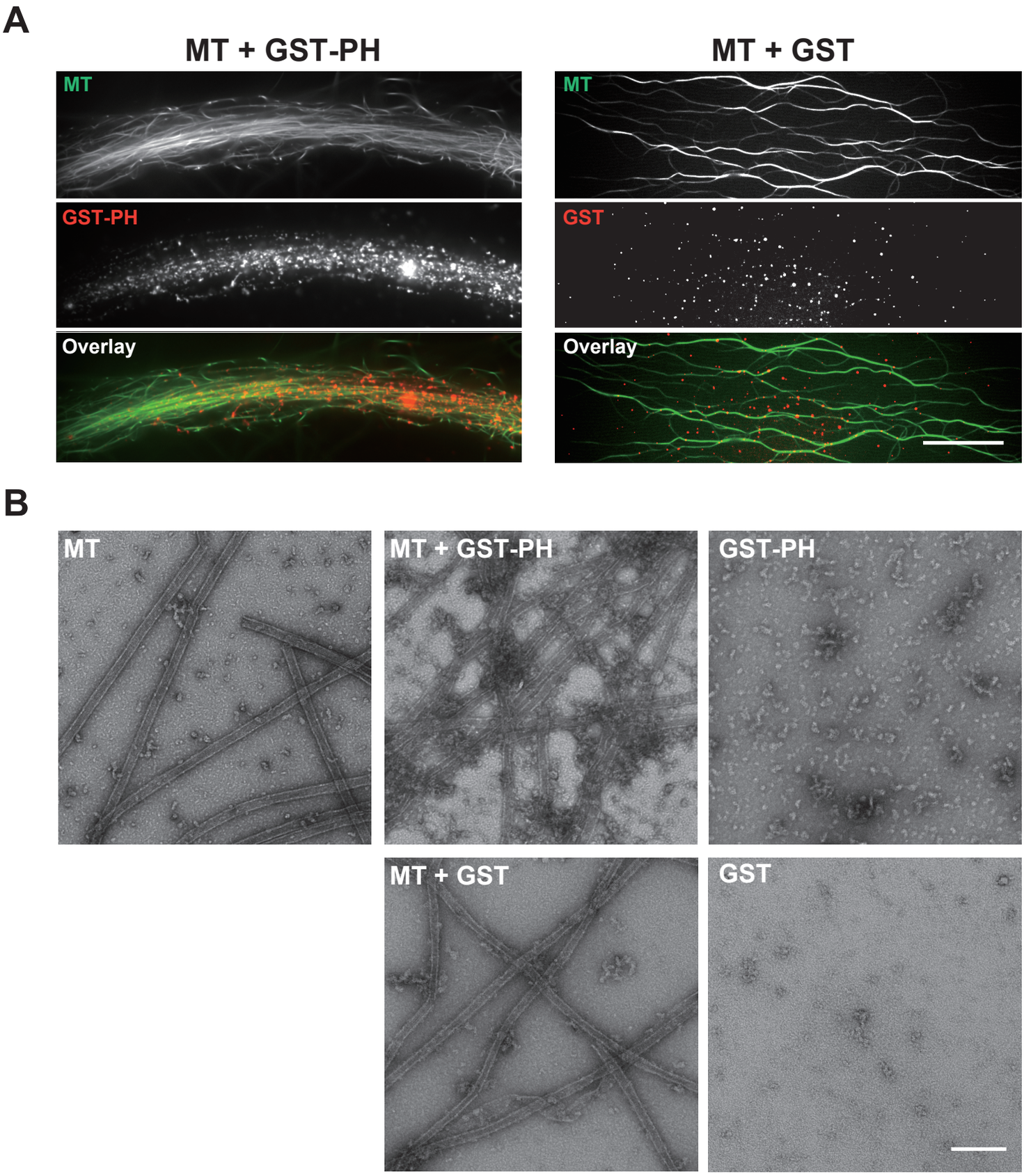
A
MT + GST-PH
MT + GST
MT
GST-PH
Overlay
MT
GST
Overlay
B
MT
MT + GST-PH
GST-PH
MT + GST
GST

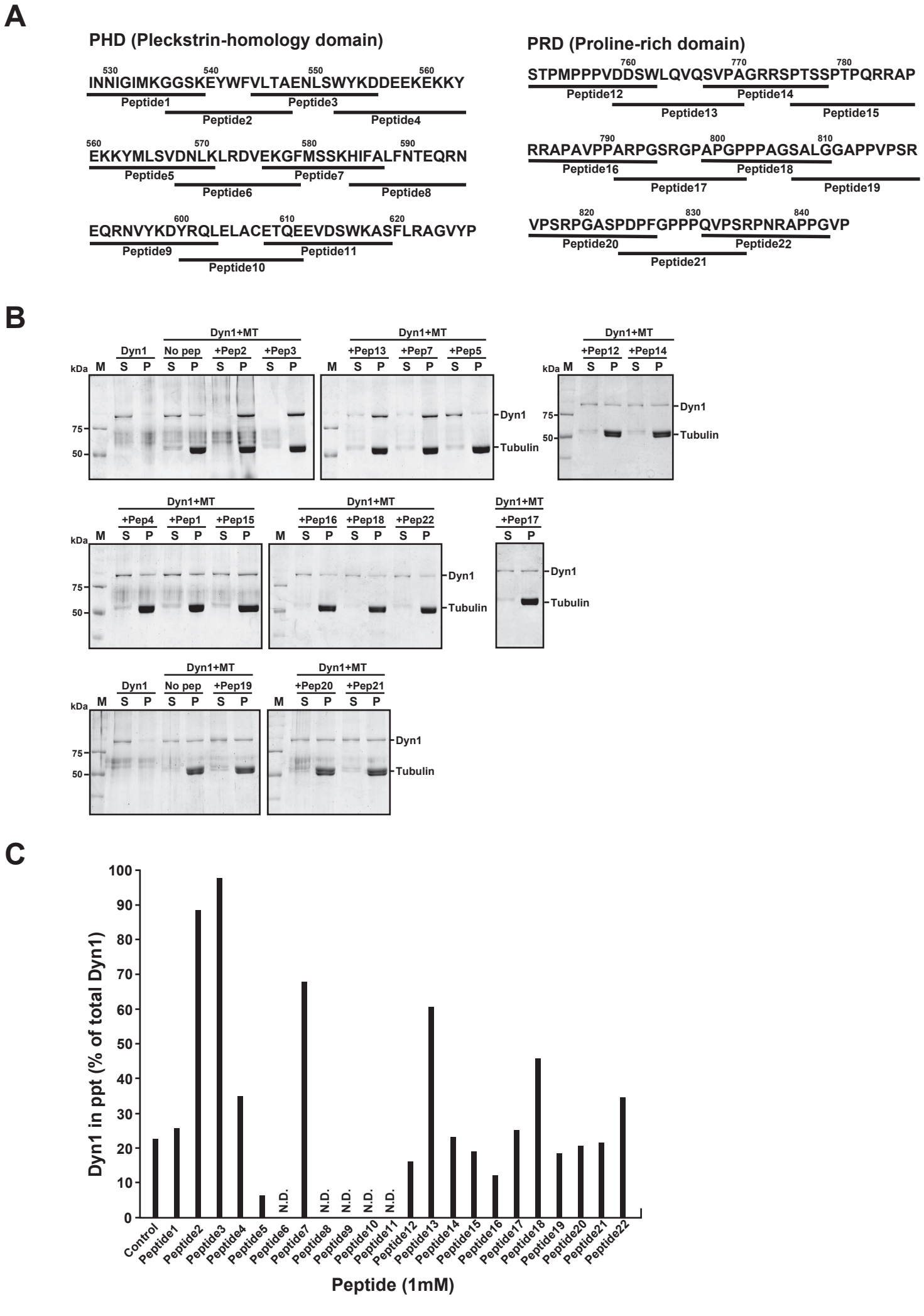
A
PHD (Pleckstrin-homology domain)
530 540 550 560
INNIGIMKGGSKEYWFVLTAENLSWYKDDEEKEKKY
Peptide1 Peptide2 Peptide3 Peptide4
560 570 580 590
EKKYMLSVDNLKLRDVEKGFMSSKHIFALFNTEQRN
Peptide5 Peptide6 Peptide7 Peptide8
600 610 620
EQRNVYKDYRQLELACETQEEVDSWKASFLRAGVYP
Peptide9 Peptide10 Peptide11
PRD (Proline-rich domain)
760 770 780
STPMPPPVDDSWLQVQSVPAGRRSPTSSPTPQRRAP
Peptide12 Peptide13 Peptide14 Peptide15
790 800 810
RRAPAVPPARPGSRGPAPGPPPAGSALGGAPPVPSR
Peptide16 Peptide17 Peptide18 Peptide19
820 830 840
VPSRPGASPDPFGPPPQVPSRPNRAPPGVP
Peptide20 Peptide21 Peptide22
B
Dyn1+MT
Dyn1 No pep +Pep2 +Pep3
+Pep13 +Pep7 +Pep5
+Pep12 +Pep14
+Pep4 +Pep1 +Pep15
+Pep16 +Pep18 +Pep22
+Pep17
+Pep19 +Pep20 +Pep21
kDa M S P
75
50
Dyn1
Tubulin
C
Dyn1 in ppt (% of total Dyn1)
100 90 80 70 60 50 40 30 20 10 0
N.D.
Control Peptide1 Peptide2 Peptide3 Peptide4 Peptide5 Peptide6 Peptide7 Peptide8 Peptide9 Peptide10 Peptide11 Peptide12 Peptide13 Peptide14 Peptide15 Peptide16 Peptide17 Peptide18 Peptide19 Peptide20 Peptide21 Peptide22
Peptide (1mM)

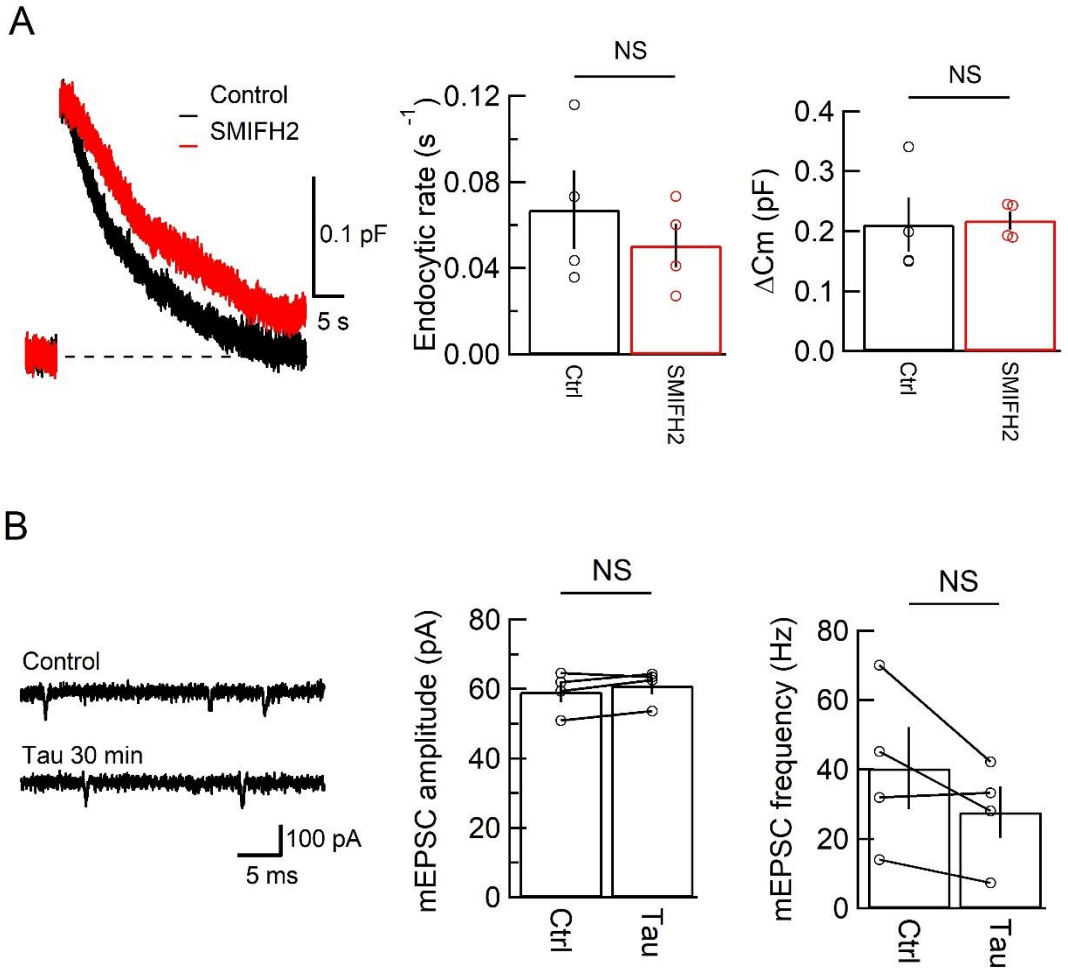
A
Control
SMIFH2
0.1 pF
5 s
NS
Endocytic rate (s-1)
0.12
0.08
0.04
0.00
Ctrl
SMIFH2
NS
ΔCm (pF)
0.4
0.3
0.2
0.1
0.0
Ctrl
SMIFH2
B
Control
Tau 30 min
100 pA
5 ms
NS
mEPSC amplitude (pA)
80
60
40
20
0
Ctrl
Tau
NS
mEPSC frequency (Hz)
80
60
40
20
0
Ctrl
Tau